Blue light generation by frequency doubling a diode laser
by Xiaoguang Sun

A dissertation submitted in partial fulfillment of the requirements for the degree of Doctor of Philosophy in Physics
Montana State University

Abstract:
In this dissertation, we present a simple scheme for construction of a low noise continuous wave blue light source by frequency doubling a Fabry-Perot diode laser in a potassium niobate crystal inside a bow tie ring cavity. By feeding back the ring cavity transmission into the diode laser after reflection off a grating, the diode laser operates in single mode and is frequency locked to the cavity resonance. Using a simple analytic form of the beam parameters for the ring cavity, the optimum cavity configuration is found for a high degree of mode matching between the diode laser output beam and the ring cavity. The wavelength of the blue output is tunable from 484-488nm, has a narrow linewidth of 1.25MHz, and has a continuous tuning range of more than 10GHz. The output power of the blue light is 18mW with intensity fluctuations less than 0.02dB. The blue light is a near diffraction limited Gaussian TEM00 mode with M2≈ Numerical simulation of the SHG is carried out by using the Fourier space method, and the experimental results are in good agreement with the simulation.

BLUE LIGHT GENERATION BY FREQUENCY DOUBLING

A DIODE LASER

by

Xiaoguang Sun

A dissertation submitted in partial fulfillment
of the requirements for the degree

of

Doctor of Philosophy

in

Physics

MONTANA STATE UNIVERSITY
Bozeman, Montana

June 2001

APPROVAL

of a dissertation submitted by

Xiaoguang Sun

This dissertation has been read by each member of the dissertation committee and has been found to be satisfactory regarding content, English usage, format, citations, bibliographic style, and consistency, and is ready for submission to the College of Graduate Studies.

Dr. John Carlsten ____________________ 6-7-01
(Signature) Date

Approved for the Department of Physics

Dr. John Hermanson ____________________ 6-11-01
(Signature) Date

Approved for the College of Graduate Studies

Dr. Bruce R. McLeod ____________________ 7-1-01
(Signature) Date

STATEMENT OF PERMISSION TO USE

In presenting this dissertation in partial fulfillment of the requirements for a doctoral degree at Montana State University, I agree that the Library shall make it available to borrowers under rules of the Library. I further agree that copying of this dissertation is allowable only for scholarly purposes, consistent with "fair use" as prescribed in the U.S. Copyright Law. Requests for extensive copying or reproduction of this dissertation should be referred to University Microfilms International, 300 North Zeeb Road, Ann Arbor Michigan 48106, to whom I have granted "the exclusive right to reproduce and distribute my dissertation in and from microform along with the non-exclusive right to reproduce and distribute my abstract in any format in whole or in part."

Signature____________________

Date 06/11/2001

ACKNOWLEDGEMENTS

I would like to thank my advisor Dr. John Carlsten for giving me the opportunity to work in his lab on this project. I am grateful for his guidance, encouragement and support.

I would like to thank Kevin Repasky, Lei Meng, Sytil Murphy, Cheryl Berger and Pete Roos for reading my paper and dissertation, making good suggestions and correcting my English.

I would like to thank Norm Williams for his help with matching.

Finally, I would like to thank my family, especially my wife, for their support.

TABLE OF CONTENTS

LIST OF TABLES

LIST OF FIGURES

ABSTRACT

In this dissertation, we present a simple scheme for construction of a low noise continuous wave blue light source by frequency doubling a Fabry-Perot diode laser in a potassium niobate crystal inside a bow tie ring cavity. By feeding back the ring cavity transmission into the diode laser after reflection off a grating, the diode laser operates in single mode and is frequency locked to the cavity resonance. Using a simple analytic form of the beam parameters for the ring cavity, the optimum cavity configuration is found for a high degree of mode matching between the diode laser output beam and the ring cavity. The wavelength of the blue output is tunable from 484-488nm, has a narrow linewidth of 1.25MHz, and has a continuous tuning range of more than 10GHz. The output power of the blue light is 18mW with intensity fluctuations less than 0.02dB. The blue light is a near diffraction limited Gaussian TEM_{00} mode with $M^2 \approx 1$. Numerical simulation of the SHG is carried out by using the Fourier space method, and the experimental results are in good agreement with the simulation.

CHAPTER-1

INTRODUCTION

Existing laser sources, such as semiconductor lasers, gas lasers, dye lasers and solid-state lasers, cover a wide range wavelengths. But many practical demands from physical, chemical and biophysical research, medical diagnostics and therapies, and environmental monitoring, require tunable coherent light sources in new spectral regions not accessible to these lasers. Examples include lithography and grating writing in the deep ultraviolet (UV) region, data storage and color display in the blue region, and ranging and pollutant detection in the infrared region. Thus it is a matter of practical importance to widen the range of wavelengths generated by the existing laser sources. For these applications, the desired features of the light sources usually include: high power, single frequency operation, narrow linewidth, low noise, good beam quality, tunability, compactness, low cost, diode pumping, all-solid-state construction for easy maintenance, and often continuous wave (CW) operation.

Significant progress has been made in the development of nonlinear optical materials for frequency conversion in recent years; a variety of new crystals with large nonlinear coefficients, large size and good optical quality are commercially available. Light sources based on nonlinear frequency conversion using these nonlinear materials to generate the desired wavelength have become practical and can meet those requirements, and even are replacing some of the existing gas lasers that are inefficient and large.

In addition, using nonlinear frequency conversion can also generate squeezed light. Squeezed state of light is a nonclassical state for which the variation in one of the two quadrature-phase amplitudes of the electromagnetic field is less than that of the vacuum state of the field. Therefore squeezed light is in some sense quieter than the light in the vacuum state and hence can be employed to improve measurement precision beyond the standard quantum limits[1].

Nonlinear frequency conversion

The basic principles of nonlinear frequency conversion are well known[1]: when an electromagnetic field propagates through a medium, the polarization of the medium can be written as a power series of the input field E

$$P = \varepsilon_0 \chi^{(1)} \cdot E + \varepsilon_0 \chi^{(2)} \cdot E^2 + \varepsilon_0 \chi^{(3)} \cdot E^3 + \ldots \qquad 1.1$$

where ε_0 is the electric permeability of vacuum, $\chi^{(1)}, \chi^{(2)}$ and $\chi^{(3)}$ are the linear, second order and third order susceptibility, and the corresponding terms are the linear, second and third order polarization, etc. As an example, suppose that if two light beams, one at frequency ω_1 and another at ω_2, are propagating in the medium. The second order polarization can be written as:

$$P^{(2)} = \varepsilon_0 \chi^{(2)} [\frac{1}{2} E_1 e^{-i\omega_1 t} + \frac{1}{2} E_2 e^{-i\omega_2 t} + cc]^2 \qquad 1.2$$

We can see that the second order polarization will have frequencies at $2\omega_1$, $2\omega_2$, $\omega_1 - \omega_2$ and $\omega_1 + \omega_2$. Radiation at new frequencies will be generated. This second order term leads to the second harmonic generation (SHG), sum frequency generation, difference frequency generation and optical parametric generation (OPG). The third order term produces frequency tripling, phase conjugation and four-wave mixing, etc.

The linear susceptibility $\chi^{(1)}$ is usually in the range of 1~10, $\chi^{(2)}$ in 10^{-12}~10^{-10} m/V, and $\chi^{(3)}$ in 10^{-21}~10^{-19} m^2/V^2.[2] To observe the nonlinear polarization, very intense light, such as that from a laser is required. Note that the absolute value of the second order susceptibility $\chi^{(2)}$ is about 9 orders of magnitude higher than that of the third order susceptibility $\chi^{(3)}$. Thus many of the practical nonlinear frequency conversion light sources are based on the second order effect, with the two most important categories being SHG and OPG.

Phase-matching

To observe a significant amount of generated light, phase matching is of vital importance. This can be explained as the following: inside the nonlinear medium, all of the induced polarization generated by the fundamental wave along its path will add coherently, and at the output of the medium, if all the waves are in phase, constructive interference will occur, and the maximum effect is achieved. On the contrary, if the phase of the generated wave adds destructively, the intensity will be diminished. A simple plane wave analysis of this nonlinear process will show that the power of the generated wave is[1]:

$$P \propto \frac{\sin^2(\Delta kL/2)}{(\Delta kL/2)^2} \qquad 1.3$$

where phase matching $\Delta k = k_1 + k_2 - k_3(\omega = \omega_1 \pm \omega_2)$, with k_1, k_2 being the wave vectors of the input waves, k_3 the generated wave, and L the length of the nonlinear medium. In general, because of the dispersion of the medium, the optical wave at different frequencies will propagate with different phase velocities, so $\Delta k \neq 0$.

One method to achieve phase matching is to utilize the birefringence of the anisotropic crystal. In the anisotropic medium, the index of refraction for a wave at a given frequency depends on the direction of propagation its as well as the polarization direction. Thus if the waves have different polarization directions, it is often possible to find a propagation direction along which phase matching is achieved.

The second method is called Quasi-phase matching (QPM)[3]. With no phase matching, maximum amplitude of the generated wave is reached after a distance l_{coh} where $\Delta k \cdot l_{coh} = \pi$. After this distance, known as coherence length, the amplitude starts to decrease because of destructive interference. But if the crystal orientation is altered, and the sign of the nonlinear coefficient is reversed, so that the next component of the generated wave is added with an additional π phase shift, then the constructive addition continues and the generated wave continues to grow. The technique for creating this kind of periodical domain inversion is known as periodic poling. The advantages of the QPM method are that phase matching can be achieved at any wavelength within the transparency range of the nonlinear material by choosing the correct period of the domain inversion, and that the largest nonlinear coefficient can be utilized. These periodically polled materials have been widely used for generating infrared light. But for generating the visible light, the domain periods required are typically between 4 μm and 7 μm, which are much smaller than that for the infrared, and are more difficult to fabricate repeatedly[4]. Thus for visible light generation, periodically polled nonlinear materials are still currently under development, so bulk crystals are still the main choice.

Continuous wave second harmonic generation

Second harmonic generation is the simplest and most familiar nonlinear interaction. The first experiment "that ushered in the field of nonlinear optics"[1] was done in 1961 by Franken et al.[5]. The early experiments were done with pulsed lasers, and the pulsed SHG could yield very high conversion efficiency (close to 100%) and a high average power[6], due to the high peak power of the pulsed laser.

For CW operation, single-pass conversion efficiency is relatively low because of the lack of high power. Resonant enhancement by an optical cavity can be used to improve the efficiency. The high circulating fundamental light plus the small beam size created by the cavity configuration can result in a high focused intensity, and therefore a high conversion efficiency. If the nonlinear crystal is placed into the same cavity with the laser gain medium, this method is called intracavity frequency doubling. Many commercial green light sources at 532nm use this method, with high efficiency over 60% and high CW power (over 10W is not uncommon).

To double a monolithic laser, such as a diode laser, the nonlinear crystal is placed in an external cavity, which is known as extracavity frequency doubling. The conversion efficiency of doubling solid-state lasers or gas lasers can reach more than 80%. For example, the highest conversion efficiency is 89% for doubling the Nd:YAG laser at

1.06 μm, and the output power of the second harmonic (SH) light more than is 1W[7]. Solid-state lasers, such as the Nd:YAG usually have relatively high powers with good spatial and spectral properties. The overall conversion efficiency of the laser is relatively low, usually within a few percents, and the wavelength tuning is limited.

Direct frequency doubling a diode laser is more attractive and can benefit from many of the desired characteristics of the diode laser. These benefits include: high efficiency, compact size, low cost, a large wavelength tuning range, etc. The efficiency of direct frequency doubling a diode laser is lower than that of doubling a solid-state laser; for example, the conversion efficiency is about 40% using a monolithic cavity[8]. Using a master oscillation passive amplification (MOPA) laser, which has a much higher output power, the efficiency can reach 58% with 1W of harmonic light[9]. In Table-1, some CW SHG experiments are listed; the conversion efficiencies are calculated with coupled fundamental power. The optical-optical efficiencies, which are calculated with the total output pump power, are lower. One of the reasons for the lowered conversion efficiency is that because of the elliptical output beam shape of laser diode, mode matching to the external resonant cavity is usually low. Using an anamorphic prism pair to change the ellipticity and other optics costs additional loss of the pump light.

For efficient SHG, the diode laser must be single longitudinal mode with a narrow linewidth, such as a distributed Bragg deflector (DBR) laser, a distributed feedback (DFB) laser or an external-cavity diode laser (ECDL). However, these are relatively expensive and sometimes difficult to obtain in the desired wavelength range, especially with high powers. As an alternative, high power Fabry-Perot diode lasers are much less expensive and easily obtainable, although these lasers are usually multimode and the linewidth of the individual modes is large (several tens to hundreds megahertz). The difficulty becomes how to achieve stable single mode operation and a narrow linewidth without losing a significant amount of the output power. One approach to narrow the linewidth is passive locking, in which the transmission from an external high-finesse cavity is fed back to the diode laser[10]. When the frequency of the of single-mode free-running diode laser is close to the cavity resonance, the laser frequency will jump to the resonance and the linewidth is also reduced by up to three orders of magnitude. For a multimode laser, to obtain single mode operation, the transmission of the external resonant cavity is fed back into the laser after reflecting off a grating. Besides the diode laser operating in a single mode, the diode laser self-locks to the ring cavity resonance.

This thesis will describe a blue light source by frequency doubling a Fabry-Perot diode laser in an external ring cavity using both cavity and grating feedback[11,12].

Overview of the thesis

This thesis is organized in four chapters. In this first chapter we have presented a short background of SHG. The external resonant cavity plays a significant role in SHG, and the efficiency depends on the mode matching, so the mode matching between the diode laser and the ring cavity is discussed in Chapter-2. In Chapter-3, the SHG is calculated using the Fourier-space method. Chapter-4 describes our blue light source by frequency doubling an infrared diode laser, and the experimental results are compared with the simulation in Chapter-3.

Table -1.1 CW SHG Experiments

Wavelength (nm)	Pump & Power	Nonlinear Crystal	Cavity	SH Power	Conversion efficiency	Reference
473	Nd:YAG 1.1W	$KNbO_3$ 5 mm	Semi-monlithic	500 mW	>81%	13
532	Miniature Nd:YAG 1.64 W	MgO:$LiNbO_3$ 7.5 mm	Semi-monlithic	1.1 W	89%	7
532	Nd:YAG 175 mW	MgO:$LiNbO_3$ 7.5mm	Standing wave monolithic	130 mW	82%	14
532	Ar^+ laser 1 W	MgO:$LiNbO_3$ 7.5 mm	Ring	0.5 W	70%	15
540	Nd:YAG 0.7W	KTP 10mm	Ring	560 mW	85%	16
266	Intracavity doubled Nd:YVO_4 500mW	BBO 12mm	Ring	100mW	22%	17
532	Nd:YAG 6.5 W	Periodically poled $LiNbO_3$ 53mm	Single pass	2.7 W	42%	18
427	External-cavity diode laser 70 mW	$KNbO_3$ 9mm	Ring	7.8 mW	34%	19
429	AR- coated Diode laser 80mW	$KNbO_3$ 6mm	Monolithic ring	14 mW	20%	20
428	Single mode diode 160 mW	$KNbO_3$ 6mm	Monolithic ring	41 mW	40%	8
465	MOPA 4W	LBO 4 mm	Ring	1W	58%	9
390	External-cavity tapered diode 1W	BBO 18mm	ring	233 mW	39%	21
403	MOPA 400mW	LBO 16mm	Ring	98 mW	25%	22
486	MOPA 740mW	$KNbO_3$ 6.5mm	Ring	156 mW	40%	23
532	α-DFB 350mW	KTP 10mm	Ring	120 mW	34%	24
421	Single mode diode 100mW	$KNBO_3$ 5mm	Ring	6.7mW	11%	25
392	External-cavity tapered diode 1W	BBO 5mm	Ring	100mW	20%	26

CHAPTER 2

BOW TIE RING CAVITY DESIGN

Bow tie ring cavities are often chosen for the external resonant field enhancement in extracavity frequency conversion experiments. The ring cavity, illustrated in Figure-2.2.1, consists of two plane mirrors M1 and M2, and two curved mirrors M3 and M4. The stable cavity mode has two beam waists: a smaller beam waist located in the center between the two spherical mirrors, where the nonlinear crystal is placed, and a larger elliptical beam waist located between the two plane mirrors. Typically the diode laser output is focused into the larger elliptical beam waist for mode matching.

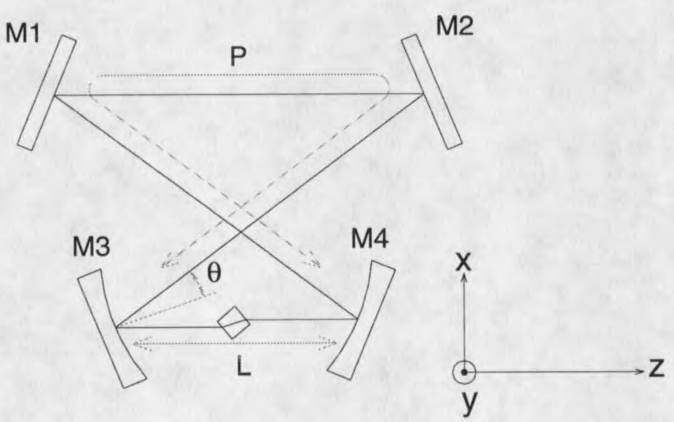

Figure-2.1 The bow tie ring cavity is formed by two plane mirrors (M1 and M2) and two spherical mirrors (M3 and M4). The incident angles on the cavity mirrors are θ, the distance between the two spherical mirrors (M3-M4) is L, and the distance between the two spherical mirrors via plane mirrors (M4-M1-M2-M3) is P.

The ring cavity has two main advantages. First, there is no direct reflection from the cavity optics back towards the diode laser so that destructive optical feedback can be avoided. Second, a uni-directional traveling harmonic wave is produced inside the cavity, which is convenient for output coupling.

Mode in a bow tie ring cavity

To maximize the efficiency of the frequency doubling, knowledge of the exact beam waist size and location inside the crystal is necessary[27]. Such analysis is usually carried out using the ABCD law and the self-consistency postulate[28,29].

Usually the bow tie ring cavity will be symmetric, with θ being the incident angle of the beam on the curved mirrors, and R the radius of the curved mirrors. As illustrated in Figure-2.1, the distance between the two curved mirrors is L, while the distance between the two curved mirrors via the two plane mirrors is P. Thus the total cavity path length is $L+P$. The complex beam parameter $q(z)$ at position z in the cavity is determined by the ABCD law for the resonator and the self-consistency postulate[2,3]:

$$q(z)=\frac{A(z)q(z)+B(z)}{C(z)q(z)+D(z)} \qquad 2.1$$

where A, B, C and D are the components of the ABCD matrix that describes one complete round-trip inside the cavity. The roots of the resulting quadratic equation of Equation-2.1 are:

$$\frac{1}{q(z)}=\frac{D-A}{2B}\pm\frac{i}{2B}\sqrt{-[(A-D)^2+4BC]} \qquad 2.2$$

Without the crystal inside the ring cavity, the ABCD matrix for a point at distance z_1 from M4, can be expressed as:

$$\begin{bmatrix} A & B \\ C & D \end{bmatrix} = \begin{bmatrix} \dfrac{f_e^{\,2} - f_e(2z_1 + P) + z_1 P}{f_e^{\,2}} & \dfrac{f_e^{\,2}(z_1 + z_2 + P) - f_e[z_1(2z_2 + P) + z_2 P] + z_1 z_2 P}{f_e^{\,2}} \\ \dfrac{P - 2f_e}{f_e^{\,2}} & \dfrac{f_e^{\,2} - f_e(2z_2 + P) + z_2 P}{f_e^{\,2}} \end{bmatrix} \quad 2.3$$

where $z_2 = L - z_1$, and f_e represents the effective focal length for the horizontal plane f_x or that for the vertical plane f_y.

At the beam waist, $\dfrac{1}{q(z)}$ is a pure imaginary number, so $D = A$. Using the expression for D and A from Equation-2.3, yields $z_1 = z_2$, which means the beam waist is at the center between the two curved mirrors. This is consistent with the symmetry of the cavity. With $z_1 = z_2 = L/2$, the beam radius ω is:

$$\omega^2 = \frac{\lambda}{2\pi}\sqrt{-\frac{4f_e^{\,2}(L+P) - 2f_e \cdot L \cdot (L+2P) + L^2 P}{P - 2f_e}} \quad 2.4$$

It is well known that a spherical mirror used at oblique incidence focuses vertical plane ray bundles at a different location than horizontal plane ray bundles. This is manifested in two different effective focal lengths f_y and f_x, where[30]

$$f_y = \frac{f}{\cos\theta} \qquad f_x = f\cos\theta \quad 2.5$$

with $f = R/2$.

With equation-2.4 and 2.5, the beam waists for the horizontal plane and the vertical plane are:

$$\omega_{0x}^{2} = \frac{\lambda \cdot f}{2 \cdot \pi} \cdot \sqrt{\frac{l - 2 \cdot \cos\theta}{p - 2 \cdot \cos\theta} \cdot [2 \cdot (l + p) \cdot \cos\theta - l \cdot p]} \qquad 2.6a$$

$$\omega_{0y}^{2} = \frac{\lambda \cdot f}{2 \cdot \pi} \cdot \sqrt{\frac{l \cdot \cos\theta - 2}{\cos\theta \cdot (p \cdot \cos\theta - 2)} \cdot [2 \cdot (l + p) - l \cdot p \cdot \cos\theta]} \qquad 2.6b$$

Here $l = \frac{L}{f}$ and $p = \frac{P}{f}$, so that L and P are normalized to f.

By using Gaussian beam propagation through a thin lens, we found that the second beam waists for the horizontal and vertical planes are located at the center of the plane mirrors, and the sizes are:

$$\omega_{0X}^{2} = \frac{\lambda \cdot f}{2 \cdot \pi} \cdot \sqrt{\frac{p - 2 \cdot \cos\theta}{l - 2 \cdot \cos\theta} \cdot [2 \cdot (l + p) \cdot \cos\theta - l \cdot p]} \qquad 2.7a$$

$$\omega_{0Y}^{2} = \frac{\lambda \cdot f}{2 \cdot \pi} \cdot \sqrt{\frac{p \cdot \cos\theta - 2}{\cos\theta \cdot (l \cdot \cos\theta - 2)} \cdot [2 \cdot (l + p) - l \cdot p \cdot \cos\theta]} \qquad 2.7b$$

Comparison of Equations 2.6 and 2.7 reveals that the result is just the exchange of l and p; this is also consistent with the structure of the cavity. In Figure-2.2 we plot the calculated beam waists in the ring cavity as a function of mirror separation p and l. We can see from the plot that ω_{0x} and ω_{0y} are generally smaller than ω_{0X} and ω_{0Y}, and the large beam waist is elliptical. By choosing the parameters l, p and θ, we can make the small beam waist circular. The sizes of the cavity beam waist are proportional to $\sqrt{R}$ as shown in Equation 2.6 and 2.7.

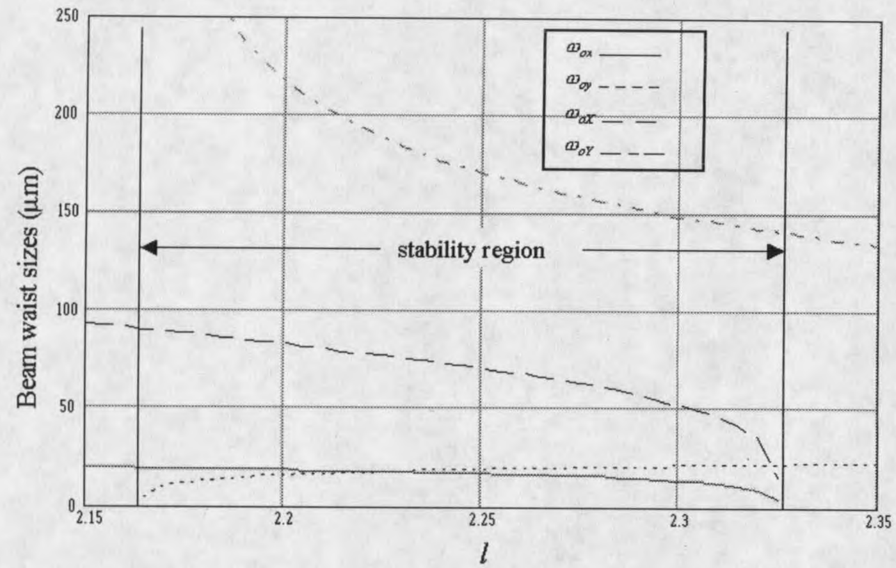

(a)

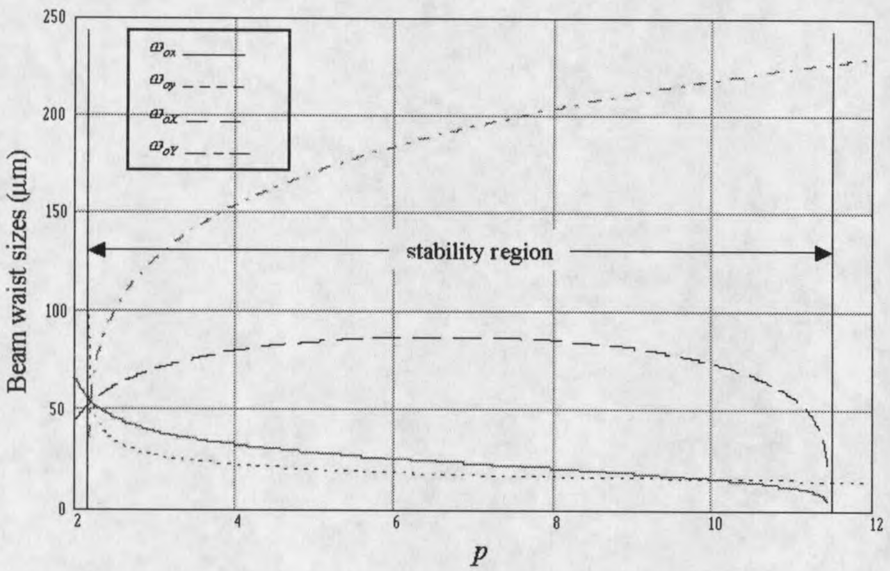

(b)

Figure-2.2 The calculated beam waists in the ring cavity as a function of mirror separation p and l using equation 2.6 and 2.7. The parameters used here are: wavelength $\lambda = 1\mu m$, radius of M3 and M4 $R = 20mm$ and angle of incidence $\theta = 22.5^{\circ}$. (a) As a function of l, with $p = 9.0$. (b) As a function of p, with $l = 2.2$. The stability region will be discussed in the next section.

Stability region and mode spot size stability of the ring cavity

From equations 2.6 and 2.7, we find that p, l and θ are confined to the stability region, which is:

$$\frac{2}{\cos\theta} < l < \frac{2p\cos\theta}{p-2\cos\theta} \qquad 2.8$$

and by the usual structure of a bow tie ring cavity, we also have

$$l < p\cos(2\theta) \qquad 2.9$$

In Figure-2.3, using equations 2.8 and 2.9, we plot the stability region for p and l. The shaded region is the stability region. When designing a bow tie ring cavity, one can use equation 2.8 to make sure p, l and θ are in the stability region.

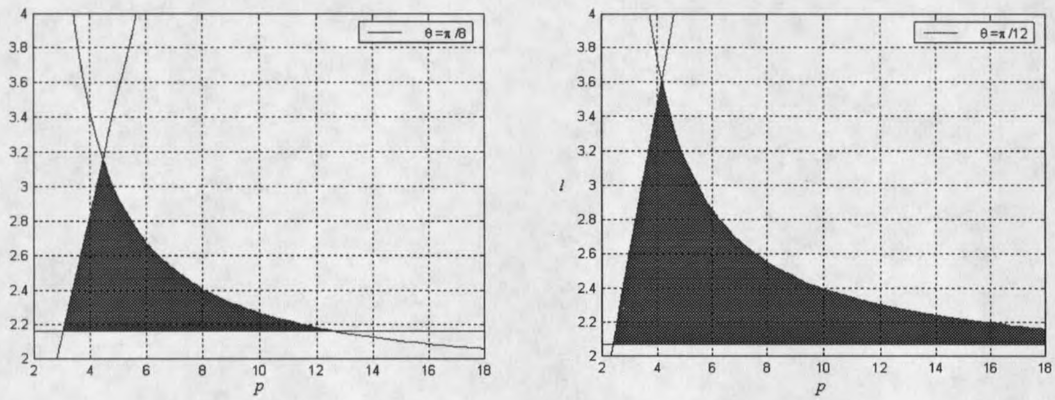

(a) (b)

Figure-2.3 The stability region of a bow tie ring cavity. (a) $\theta = 22.5^{o}$, (b) $\theta = 15^{o}$. The shaded region is determined by equation (8) and (9). A smaller folding angle has a larger stability region.

Also when we choose the parameters p, l and θ, it is important that the cavity is not near the edge of the stability region, because near the edge, the beam size is critical to small variations of the parameters. As in reference [28], the mode spot size stability can be calculated using:

$$\frac{1}{\omega}\frac{\partial \omega}{\partial x} \qquad 2.10$$

where ω is the beam waist size, either $\omega_{0x}, \omega_{0y}, \omega_{0X}$ or ω_{0Y}, and x is one of the parameters, either p, l or θ. From the derivatives for $\omega_{0x}, \omega_{0y}, \omega_{0X}$ and ω_{0Y} and Figure-2.2, it is easy to see that when p and l are in the center of the stability region, the changes are small, and the most critical parameter is the distance l.

Mode with the crystal

If a crystal is placed between the two spherical mirrors, the effective length between the two spherical mirrors is changed. In addition, the crystal will need to be rotated to achieve phase matching (see Appendix C). Since we will rotate the crystal in the horizontal plane, the tilted crystal will act differently on the horizontal and the vertical ray bundles. Thus the effective distances which the rays propagate in the horizontal and the vertical plane are different [31], and are given by:

$$d_x = \frac{t \cdot n^2 (1 - \sin^2 \phi)}{(n^2 - \sin^2 \phi)^{3/2}}$$
$$d_y = \frac{t}{\sqrt{n^2 - \sin^2 \phi}} \qquad 2.11$$

The derivation of equation 2.11 is given in Appendix A. Here n is the refractive index of the crystal, ϕ is the incident angle on the crystal, $t = \frac{T}{f}$, and T is the length of the crystal. Note that d_x and d_y are still normalized to the focal length f as before. Thus the effective distances between the two spherical mirrors in the horizontal plane and the vertical plane are:

$$l_x = l + \frac{t \cdot n^2(1-\sin^2\phi)}{(n^2-\sin^2\phi)^{3/2}} - t\sqrt{1-\sin^2\phi} - \frac{t\sin^2\phi}{\sqrt{n^2-\sin^2\phi}}$$
$$l_y = l + \frac{t}{\sqrt{n^2-\sin^2\phi}} - t\sqrt{1-\sin^2\phi} - \frac{t\sin^2\phi}{\sqrt{n^2-\sin^2\phi}} \qquad 2.12$$

Therefore the beam waist sizes with the tilted crystal can be obtained by replacing l in equations 2.6a and 2.7a with l_x and also by replacing l in equations 2.6b and 2.7b by l_y. The location of the larger beam will always remain at the center between the plane mirrors, and that of the smaller beam waist will locate at the center of the crystal when the crystal is placed halfway between the spherical mirrors. When the crystal is moved from the halfway point between the spherical mirrors, the location of the smaller beam waist will also move away from the center of the crystal. The smaller beam waist should be located at center of the crystal to maximize the nonlinear conversion efficiency, especially for a tightly focused beam.

As shown in Figure-2.4, if the crystal is placed a distance Δ from the center between the two curved mirrors, the beam waist will locate at a distance x from the center of the crystal. It is easy to show that if $\Delta < d_e/2$, where d_e represent either d_x or d_y, the beam waist will locate inside the crystal, and

$$x = \frac{t_2}{d_e}\Delta \qquad 2.13$$

with $t_2 = t\sqrt{1-\sin^2\phi} + \dfrac{t\sin^2\phi}{\sqrt{n^2-\sin^2\phi}}$.

If $\Delta > d_e/2$, the beam waist will locate outside the crystal and

$$x = \Delta + \frac{t_2}{2} - \frac{d_e}{2} \qquad 2.14$$

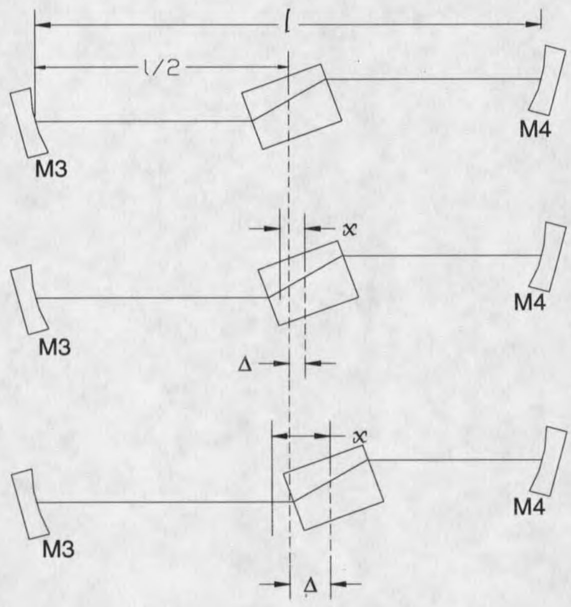

Figure-2.4 If the crystal is placed a distance Δ from the center between the two curved mirrors, the beam waist will locate at a distance x from the center of the crystal. When $\Delta < d_e/2$, the beam waist will locate inside the crystal, and $\Delta > d_e/2$, the beam waist will locate outside the crystal.

Because the effective distances between the two spherical mirrors in the horizontal plane and the vertical plane have changed, the stability region becomes:

$$\frac{2}{\cos\theta} < l_x,\ l_y < \frac{2p\cos\theta}{p-2\cos\theta} \qquad 2.15$$

Mode matching between the diode laser and the ring cavity

From Equations 2.6 and 2.7 and Figure-2.2, it is easy to show that the beam waist between the two plane mirrors is larger and elliptically shaped. The output beam of a diode laser usually has an elliptical Gaussian shape, so the focused beam waist will also be elliptical. To mode match the diode laser output beam to the external cavity, an anamorphic prism is often used to reduce the ellipticity. But the anamorphic prism will introduce insertion loss and unwanted back reflection into the laser, which can cause instability of the diode laser. A better way to efficiently mode match the diode output into the ring cavity is to adjust the parameters of the ring cavity so that the sizes of the larger elliptical beam waist of the ring cavity are the same as those of the focused diode laser output beam in both the vertical and horizontal plane. And at the same time, the smaller beam waist can be circular for efficient SHG.

Assume that the beam waists are ω_x^0 and ω_y^0 at the output of the diode laser for the horizontal and the vertical plane. If two lenses, with focal length f_1 and f_2 respectively, are used to focus the beam into the ring cavity, illustrated in Figure-2.5, the separation of the two lenses is $f_1 \frac{d}{d-f_1} + f_2$, with d the distance between the first lens L1 and the diode laser, it is easy to show that when $d - f_1 >> \frac{\pi(\omega_i^0)^2}{\lambda}$; the focused beam waist sizes after lens L2 are:

$$\omega_i = \frac{\lambda}{\pi} \frac{f_2}{f_1} \frac{d-f_1}{\omega_i^0} \qquad i = x, y \qquad 2.16$$

The beam waist location is f_2 behind lens L2. Thus the ellipticity of the focused output beam is the same as that of the diode laser, and the size depends on $d - f_1$. The astigmatism of the diode laser will slightly change this result, which shall be considered. In the experiment it is usually necessary to keep the distance from the diode laser to the output focus short; thus a larger d and shorter f_1 and f_2 are favored.

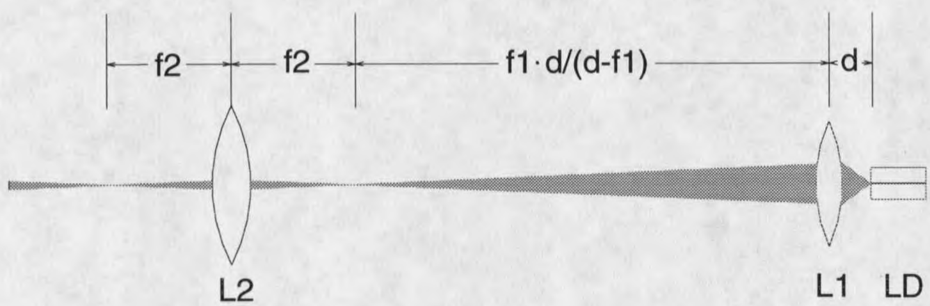

Figure-2.5 Focus the diode laser output by two spherical lenses. The lens L1 is d from the diode laser, the focused beam is $f_1 \dfrac{d}{d - f_1}$ behind the L1 and f_2 behind L2.

The ellipticity of the diode laser can vary with device design, and is usually in the range between 2~3. To change the ellipticity of the large beam waist, we could change l, p and the incident angle θ. It is more desirable to vary θ and keep l and p in the region where the beam waists change slowly with l and p, as discussed in the previous section.

As an example, in Figure-2.6 we plot the solutions where the large beam waist has an ellipticity of 1:2.7, and the smaller beam waist is kept circular. Because we have two equations,

$$\begin{aligned} \omega_{0Y} / \omega_{0X} &= 2.7 \\ \omega_{0y} / \omega_{0x} &= 1 \end{aligned} \qquad 2.17$$

there will exist a set of solution l and p for each incident angle θ.

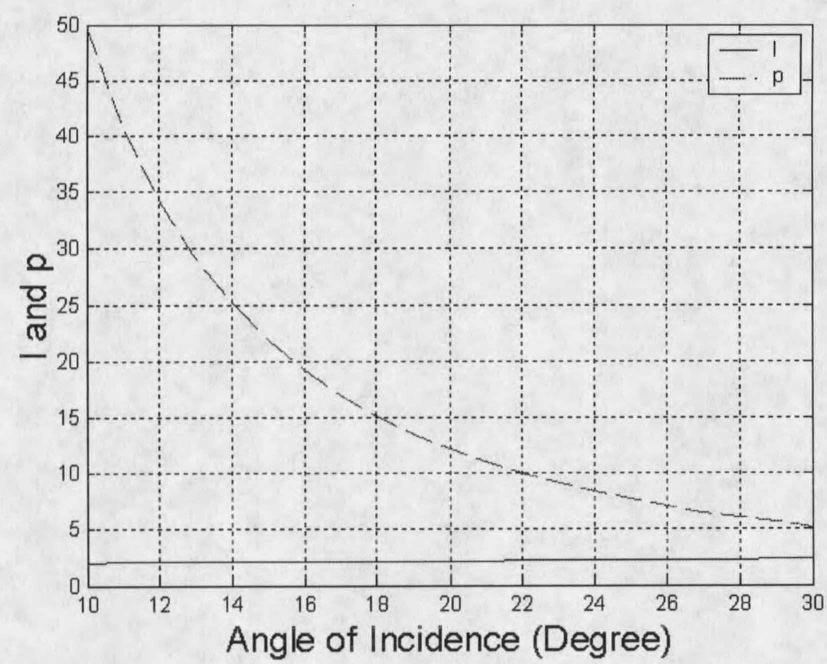

(a)

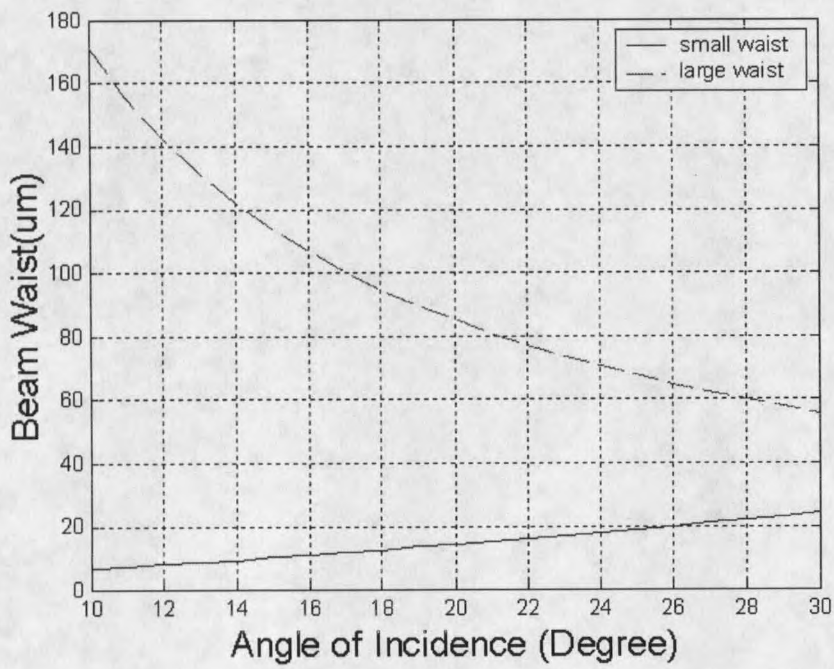

(b)

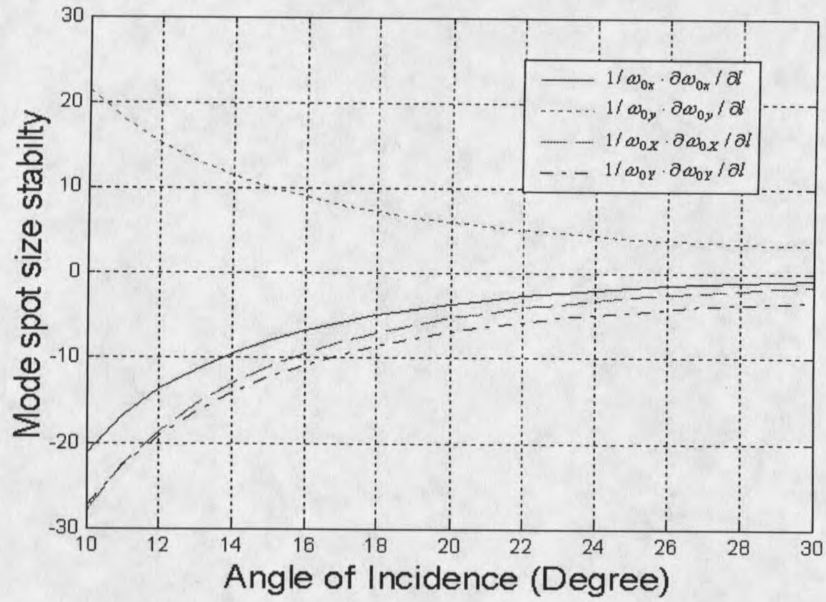

(c)

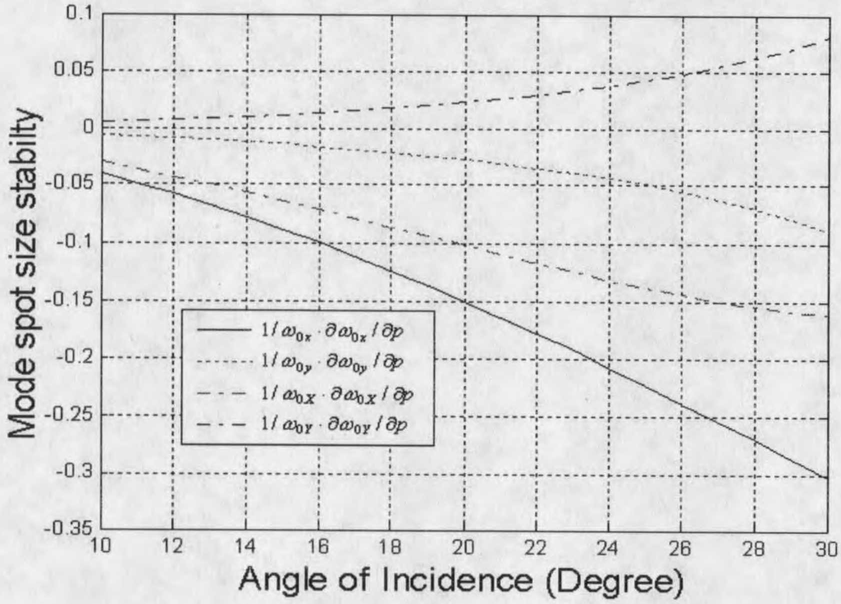

(d)

Figure-2.6 The solution for the large beam waist size with an ellipticity of 1:2.7, and the small beam is circular with different incident angle θ. (a) The solution of l and p. (b) Horizontal beam waist size ω_{0X} and ω_{0x}. The mode spot size stability calculated using Equation 2.10 (c) for ω_{0x}, ω_{0y}, ω_{0X} and ω_{0Y} with l. (d) ω_{0x}, ω_{0y}, ω_{0X} and ω_{0Y} with p.

Figure-2.6 (a) plots the solution of l and p as a function of incident angles θ. At each angle, the beam waist sizes are also determined. The horizontal beam waist size ω_{0X} and ω_{0x} are plotted in Figure-2.6 (b). The vertical beam waist size of ω_{0Y} and ω_{0y}, which are also determined by Equation-2.16 are omitted for simplicity. The mode spot size stability for both beam waists in both horizontal and vertical planes are calculated using Equation 2.10. In Figure-2.6 (c) the mode spot size stability with respect to the distance l are plotted. In Figure-2.6 (d) the mode spot size stability with respect to the distance p are plotted. The parameters in our calculation are: $\lambda = 1\mu m$, $R = 20mm$.

We can see from (c) and (d) that the mode spot size stabilities with p are one order of magnitude smaller than those with l. Therefore our primary concern is for the mode stability with l. Looking at Figure-2.6 (c) it is clear that a larger folding angle is preferred for smaller mode size stability values. We chose to operate with an incident angle θ=22.5°. This choice has several benefits. First, the mode spot size stabilities for l are low. Second, the value of p is also reduced, which shortens the total cavity length, and increases the free spectral range (FSR) of the cavity.

From these plots, we can see that by adjusting the parameters of the ring cavity we can obtain the desired ellipticity and can match the output of the diode laser to the cavity mode without an anamorphic prism. In addition, by a judicial choice of θ, other benefits of good mode stability and larger FSR can be obtained.

Cavity tuning for large frequency scanning range

In the experiments, the resonance of the external bow tie ring cavity needs to be changed continuously. This tuning is usually accomplished by moving one of the mirrors, thus changing the total length of the cavity. But this movement will increase the misalignment of the resonator due to the change of the beam path, as illustrated in Figure-2.7 (a), and cause a reduction of the finesse and the enhancement. This will cause another problem in our experiment, which an extra grating is utilized to provide filtered optical feedback. As the beam path inside the cavity changes, the feedback phase, the center wavelength and shape of the grating feedback can also be changed. Thus the system will lose locking.

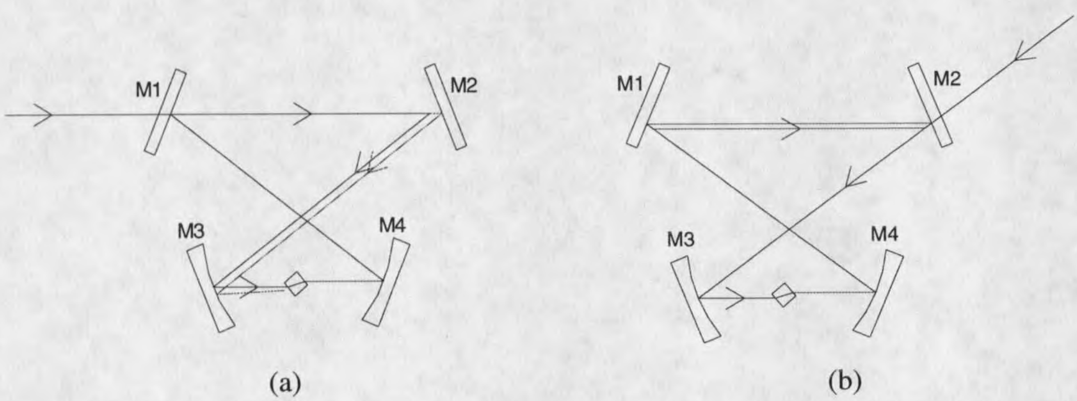

Figure-2.7 Cavity tuning of a bow tie ring cavity. (a) If only M2 is moved, a misalignment will occur. (b) if M1 and M2 is moved simultaneously upward, there will be no misalignment.

Instead, if we move the two plane mirrors simultaneously, as illustrated in Figure-2.7 (b), there will be no misalignment of the beam by changing the length of the cavity. It is easy to show that when the M1 and M2 move a distance h upward, the total cavity length change will be:

$$\Delta_c = 2h\left(\frac{1+\dfrac{1}{\cos 2\theta}}{\tan 2\theta + \dfrac{1}{\tan\theta}}\right) \tag{2.16}$$

CHAPTER 3

SHG CALCULATION USING THE FOURIER-SPACE METHOD

Though the SHG is the simplest nonlinear process, the interaction can be complex. Obtaining accurate results of the SHG is difficult because there are many effects that will complicate the calculation. These effects include the following:

a) The fundamental beam is usually tightly focused to a small diameter in order to increase its intensity and hence to achieve a higher efficiency. Therefore the intensity profile is not uniform but has a Gaussian or other complex distribution. Thus the intensity profile and diffraction effects cannot be ignored.

b) When birefringence is utilized to achieve phase matching inside the birefringent medium, the wave vectors of the fundamental and the SH wave are in the same direction, but the Poynting vectors of the corresponding fields are not. Thus the beams will separate from each other as they travel through the medium, and the nonlinear process is diminished. This effect, known as "Poynting vector walk-off", will be an important factor and will limit the efficiency of the SHG and affect the waveform of the SH wave.

c) With the availability of high power lasers, the large enhancements of the external cavities, and the availability of large nonlinear coefficient crystals with relatively large sizes, the conversion efficiency can be high. Therefore the effect of beam depletion has to be considered.

d) Because each plane-wave component of the waves has different refractive index in the birefringent nonlinear medium, phase matching cannot be achieved simultaneously for all the plane-wave components. Thus the phase matching condition can be much different from that given by the simple plane-wave analysis.

Besides calculating the conversion efficiency, we need to know the transverse beam profile of the generated SH wave, and to evaluate the beam quality when the effects mentioned above can complicate the waveforms of both waves.

When some of the above mentioned effects could be ignored, analytic results can be obtained. For example, the plane-wave model for calculating the SHG is valid when the diffraction and the walk-off can be ignored. Boyd and Kleiman calculated the SHG process including walk-off and diffraction of the fundamental wave but the depletion is ignored[33]. These calculations concentrate on the conversion, but the beam profiles for the SH wave were not calculated.

To include all these effects and to calculate the beam profile, numerical methods are necessary. Several computation methods have been proposed[34,35,36,37]. One numerical method is the Fourier-space method[36,37], first proposed by Sheng and Siegman. Arisholm extended this method to the biaxial crystal. In this method, the electromagnetic waves are decomposed into the plane-wave eigenmodes of the birefringence crystal, and then the coupled nonlinear differential equations for the slowly varying amplitudes of each plane-wave are solved. The walk-off and the phase mismatch of the different plane-wave components are associated with the birefringence of the crystal. Thus by including the exact refractive index associated with each plane-wave, these effects are included in the coupled differential equation. But in their papers, REF[36] and [37], the coupled differential equations for the SHG are not exact and phase mismatching is not discussed. It is known that for the SHG with focused Gaussian beams, the maximum conversion efficiency does not occur at the phase matching condition $\Delta k = 0$, but at a Δk larger than zero.

First we will give a rigorous derivation of the coupled differential wave equations for the SHG. Then the procedures to solve the equations by Runge-Kutta method and simulation of the SHG are described, and the results are given.

Mathematical development

The electromagnetic field propagating in the z -direction can be written as:

$$\vec{E}(x,y,z,t) = \frac{1}{2}(\hat{e}E(x,y,z)e^{-i(\omega t - kz)} + cc) \tag{3.1}$$

$\hat{e}$ is the polarization unit vector of the electromagnetic field. $E(x,y,z)$ is slowly-varying along the z -direction, and can be transformed using the two dimensional Fourier transformation[36, 38]:

$$\begin{aligned} E(x,y,z) &= \frac{1}{(2\pi)^2}\iint dk_x dk_y \tilde{e}(k_x,k_y,z)e^{i[k_z(k_x,k_y)-k]z}\cdot e^{i(k_x x + k_x y)} \\ \tilde{e}(k_x,k_y,z) &= e^{-i[k_z(k_x,k_y)-k]z}\iint dxdy E(x,y,z)\cdot e^{-i(k_x x + k_x y)} \end{aligned} \tag{3.2}$$

with $k_z(k_x,k_y) = \sqrt{k^2(k_x,k_y) - (k_x{}^2 + k_y{}^2)}$, and $k(k_x,k_y) = n(k_x,k_y)2\pi/\lambda$, λ is the wavelength in free space, and $n(k_x,k_y)$ the refractive index, which is dependent on the direction of propagation and polarization, and $k = n2\pi/\lambda$, with n the refractive index for a plane wave propagation in the z-direction.

Starting from the Maxwell's wave equations in nonmagnetic media:

$$\nabla^2\vec{E}(x,y,z,t) - \nabla(\nabla\cdot\vec{E}(x,y,z,t)) - \mu_0\frac{\partial^2\vec{P}_L(x,y,z,t)}{\partial t^2} = \mu_0\frac{\partial^2\vec{P}_{NL}(x,y,z,t)}{\partial t^2} \qquad 3.3$$

$\vec{E}$ is the electromagnetic wave inside the crystal consisting of the fundamental wave and the SH wave:

$$\vec{E}(x,y,z,t) = \frac{1}{2}(\hat{e}_1 E_1(x,y.z)e^{-i(\omega t-k_1 z)} + \hat{e}_2 E_2(x,y.z)e^{-i(2\omega t-k_2 z)} + cc) \qquad 3.4$$

where $k_1 = \frac{2\pi}{\lambda}n^{\omega}$, $k_2 = \frac{4\pi}{\lambda}n^{2\omega}$, λ is the wavelength of the fundamental wave, n^{ω} and $n^{2\omega}$ are the refractive index inside the crystal at the fundamental and the SH frequency.

To achieve the phase-matching condition, the fundamental wave and the SH wave will have orthogonal polarizations. Thus $\hat{e}$ is either one of the two eigenmodes polarization directions for the wave propagating in the z-direction. Thus the vector nature of the electromagnetic waves can be simplified as discussed in Appendix-B.

In Equation 3.3, the linear polarizations are:

$$\begin{aligned}\vec{P}_{Lj}(x,y,z,t) &= \frac{1}{2}(\hat{e}_j P_{Lj}(x,y.z)e^{-i(\omega_j t-k_j z)} + cc)\\ P_{Lj}(x,y,z) &= \frac{1}{(2\pi)^2}\int\int dk_x dk_y n_j^{\,2}(k_x,k_y)\cdot\tilde{e}_j(k_x,k_y,z)e^{i[k_{jz}(k_x,k_y)-k_j]z}\cdot e^{i(k_x x+k_x y)}\end{aligned} \qquad 3.5$$

with $j=1$ and 2 for the fundamental wave and the SH wave respectively.

The nonlinear polarizations are: $\vec{P}_{NLj} = \hat{e}_j P_{NLj}$, with $j = 1$ and 2. Because of the phase matching, only the nonlinear polarization along the electromagnetic field needs to be considered. For the fundamental wave:

$$\begin{aligned} P_{NL1}(x,y,z) &= 2\varepsilon_0 d_{eff} E_1^*(x,y,z) E_2(x,y,z) \\ &= 2\varepsilon_0 d_{eff} \left[\frac{1}{(2\pi)^2} \iint dk_x dk_y \tilde{e}_1(k_x,k_y,z) e^{i[k_{1z}(k_x,k_y)-k_1]z} \cdot e^{i(k_x x + k_x y)} \right]^* \\ &\quad \cdot \left[\frac{1}{(2\pi)^2} \iint dk_x dk_y \tilde{e}_2(k_x,k_y,z) e^{i[k_{2z}(k_x,k_y)-k_2]z} \cdot e^{i(k_x x + k_x y)} \right] \\ &= \frac{1}{(2\pi)^2} \iint dk_x dk_y \tilde{P}_{NL1}(k_x,k_y,z) e^{i[k_{iz}(k_x,k_y)-k_1]z} \cdot e^{i(k_x x + k_x y)} \end{aligned} \quad 3.6$$

$$\tilde{P}_{NL1}(k_x,k_y,z) = 2\varepsilon_0 d_{eff} \cdot \tilde{e}_1(-k_x,-k_y,z) e^{-i[k_{1z}(k_x,k_y)-k_1]z} \otimes \tilde{e}_2(k_x,k_y,z) e^{i[k_{2z}(k_x,k_y)-k_2]z}$$

$\otimes$ denotes convolution[6], and d_{eff} is the effective nonlinear coefficient, discussed in Appendix-C.

And similarly for the SH wave:

$$\begin{aligned} P_{NL2}(x,y,z) &= \varepsilon_0 d_{eff} [E_1(x,y,z)]^2 \\ &= \varepsilon_0 d_{eff} \left[\frac{1}{(2\pi)^2} \iint dk_x dk_y \tilde{e}_1(k_x,k_y,z) e^{i[k_{1z}(k_x,k_y)-k_1]z} \cdot e^{i(k_x x + k_x y)} \right]^2 \\ &= \frac{1}{(2\pi)^2} \iint dk_x dk_y \tilde{P}_{NL2}(k_x,k_y,z) e^{i[k_{2z}(k_x,k_y)-k_2]z} \cdot e^{i(k_x x + k_x y)} \end{aligned} \quad 3.7$$

$$\tilde{P}_{NL2}(k_x,k_y,z) = \varepsilon_0 d_{eff} \cdot \tilde{e}_1(k_x,k_y,z) e^{i[k_{1z}(k_x,k_y)-k_1]z} \otimes \tilde{e}_1(k_x,k_y,z) e^{i[k_{1z}(k_x,k_y)-k_1]z}$$

Plugging Equation-3.6 and -3.7 into Equation-3.3, and using the slowly varying amplitude approximation, we found the coupled differential equations for the two beams:

$$\frac{\partial \tilde{e}_1(k_x,k_y,z)}{\partial z} = id_{eff}\frac{\omega^2}{c^2}\frac{1}{k_{1z}}e^{-i\Delta k\cdot z}e^{i(k_1-k_{1z})\cdot z}$$
$$\cdot\left[\tilde{e}_1^*(-k_x,-k_y,z)e^{-i[k_{1z}(k_x,k_y)-k_1]z}\otimes\tilde{e}_2(k_x,k_y,z)e^{i[k_{2z}(k_x,k_y)-k_2]z}\right]$$
$$\frac{\partial \tilde{e}_2(k_x,k_y,z)}{\partial z} = i2d_{eff}\frac{\omega^2}{c^2}\frac{1}{k_{2z}}e^{i\Delta k\cdot z}e^{i(k_2-k_{2z})\cdot z} \qquad 3.8$$
$$\cdot\left[\tilde{e}_1(k_x,k_y,z)e^{i[k_{1z}(k_x,k_y)-k_1]z}\otimes\tilde{e}_1(k_x,k_y,z)e^{i[k_{1z}(k_x,k_y)-k_1]z}\right]$$

where $\Delta k = 2k_1 - k_2 = \frac{4\pi}{\lambda}[n^{\omega}(k_x=0,k_y=0)-n^{2\omega}(k_x=0,k_y=0)]$.

Because of the small walk-off angle the longitudinal components of the electromagnetic waves are ignored as discussed in Appendix-B

As discussed in REF[5], one doesn't need to assume which one of the fundamental and the SH waves is e-wave and o-wave (or *fast*-wave and *slow*-wave); the birefringence properties of the waves are included with the dependence of the refractive index on the propagation direction, i.e. $n = n(k_x,k_y)$.

Numerical simulation of SHG in a $KNbO_3$ crystal

For the wavelength near 970 nm at room temperature, the phase matching condition is achieved when the fundamental beam is propagating in the X-Y plane and the polarization direction is also in the X-Y plane. The polarization of the generated SH wave is in the Z-direction. This configuration gives the maximum effective nonlinear coefficient d_{eff} and the smallest walk-off near 970 nm at room temperature. The walk-off is in the horizontal plane and walk-off angle is ρ =0.0094. The walk-off is discussed in

Appendix B. The properties of the $KNbO_3$ crystal and phase matching are given in Appendix-C.

Assume that the fundamental wave is an elliptic Gaussian beam, and the beam waist is located at a distance $l_{w,x}$ and $l_{w,y}$ from the front surface of the crystal for the horizontal and the vertical plane, as illustrated in Figure-3.1. The initial input beams are that the fundamental wave at the front surface of the crystal is:

$$E_1(x,y,z=0)=\frac{E_0}{\sqrt{1+i\zeta_x}\sqrt{1+i\zeta_y}}\exp\left[-\frac{x^2}{\omega_{0,x}{}^2(1+i\zeta_x)}-\frac{y^2}{\omega_{0,y}{}^2(1+i\zeta_y)}\right] \qquad 3.9$$

with $\zeta_i = 2(z-l_{w,i})/b_i$, the confocal parameter $b_i = k_1\omega_{0,i}{}^2$, and $\omega_{0,i}$ the radius of the beam waist, $i = x, y$ for the horizontal and the vertical plane,. The initial input for the SH wave is

$$E_2(x,y,z=0)=0 \qquad 3.10$$

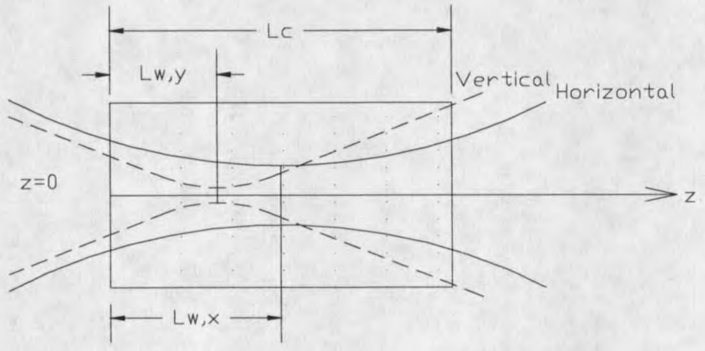

Figure-3.1 The input fundamental wave and the nonlinear crystal. The crystal length is L_c, the input elliptical Gaussian fundamental wave has beam waists of $\omega_{0,x}$ and $\omega_{0,y}$ for the horizontal and the vertical plane, located at $l_{w,x}$ and $l_{w,y}$ behind the crystal's front surface respectively.

In the following simulations, we will assume $\omega_{0,x} = \omega_{0,y} = \omega_0$ and $l_{w,x} = l_{w,y} = l_w$ for simplicity. For each of the waves, usually the transverse field at position z is represented by a 256X256 matrix with $\omega_0 / 8$ resolution. The z-direction is usually sliced to 16 sections, within each section, the wave Equation-3.8 is solved by the fifth-order Runge-Kutta method[39]. At end of each section, with the SH wave $E^{2\omega}$ calculated, the $E^{2\omega}$ is then fitted to the Gaussian distribution:

$$\left|E^{2\omega}(x,y)\right| = E_0 \exp\left[-\frac{(x-x_p)^2}{\omega_x^{\,2}(z)} - \frac{(y-y_p)^2}{\omega_y^{\,2}(z)}\right] \qquad 3.11$$

with $\omega_x(z)$ and $\omega_y(z)$ the beam waist in the horizontal and the vertical plane, x_p, y_p the peak position and E_0 the amplitude.

We can use a smaller matrix to represent the transverse electromagnetic field when the fundamental wave has a larger beam waist. For example, a 128X128 matrix with $\omega_0 / 6$ resolution can be used for a fundamental beam with a waist size of over 20 μm. The number of slices in z-direction is determined by the interaction strength of the SHG. A good indication of the strength is the interaction length[40], defined as

$$L_{NL} = \frac{n\lambda_1}{2\pi \cdot d_{eff} E_0} \qquad 3.12$$

For a plane wave fundamental light with amplitude E_0, 58% conversion efficiency will be reached over this interaction length. Although the conversion efficiency is lower for the Gaussian beams, L_{NL} is still a good indication of by the interaction strength. With the crystal length $Lc > L_{NL}$, more slices are necessary to maintain the accuracy. The typical calculation time is about 10 minutes in a Pentium PC using MATLAB.

A few methods are used to check the accuracy of the calculation. The total power of the fundamental and the SH at the output is compared with that at the input. Without absorption, this should be constant. The difference is usually within 10^{-8}.

As in REF[4], for a plane wave input, the calculated conversion efficiency is compared with the theory[1]. When the input fundamental is a plane wave, the conversion efficiency is given by:

$$\eta(L_c) = \tanh^2(L_c / L_{NL}) \qquad 3.12$$

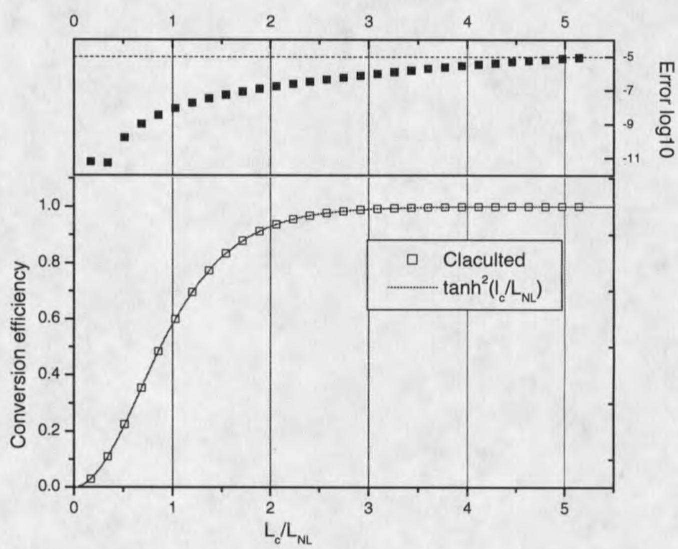

Figure-3.2 Conversion efficiency of the calculated and theory of a plane wave model, the error is within 10^{-5}.

The results of the simulation are shown in Figure-3.3.2. The error is within 10^{-5} for 16 slices of the crystal. As we can see from Figure-3.3.2, the error increases for longer crystal length. Smaller steps or adaptive-steps are necessary to increase the accuracy, but also will require more time for the computation.

Phase mismatching and the SH power

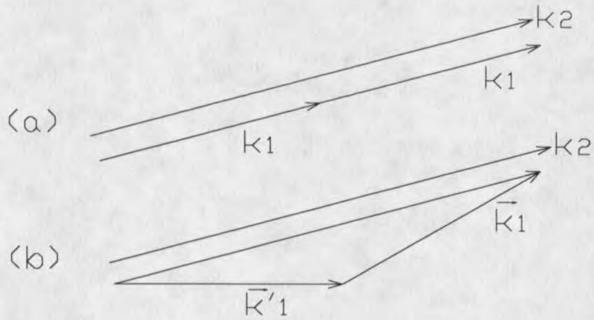

Figure-3.3 A positive phase mismatching is needed for maximum conversion of focused Gaussian beams. (a) collinear SHG, when $k_2 = 2k_1$, maximum SH is reached. (b) non-collinear SHG, when $k_2 = \left|\vec{k}_1 + \vec{k}'_1\right|$, maximum SH is reached, which requires $k_1 > \frac{k_2}{2}$.

For the SHG with focused Gaussian beams, the maximum conversion is achieved with a positive phase mismatch $\Delta k > 0$. Boyd explained that this is caused by the phase shift of π radians the beam experiences in passing through the focus[2]. But it easy to show that if the focus is outside the crystal, a positive phase mismatch $\Delta k > 0$ is still needed for the maximum conversion. An alternative explanation would be that because each wave consists of plane-wave components of different directions, both collinear and non-collinear interactions occur for the SHG, as illustrated in Figure-3.3. For the collinear SHG, when $\Delta k = 2k_1 - k_2 = 0$, the maximum conversion is achieved. For the non-collinear SHG, the maximum conversion is achieved when $(\vec{k}_1 + \vec{k}_1') \cdot \hat{k}_2 = |k_2|$. Because $|\vec{k}_1 + \vec{k}_1'| < 2|k_1|$, a positive $\Delta k = 2k_1 - k_2 > 0$ is required.

REF[41] discussed the phase mismatching of the SHG with focused Gaussian beams. They assumed that the fundamental and the SH wave were both Gaussian beams, which is valid when the walk-off and the depletion can be ignored. The walk-off can affect the SH transverse beam shape, and make the Gaussian beam assumption less accurate, especially for tightly focused beams. We plot the beam sizes of the SH wave inside the crystal in Figure-3.4 (a). It can be seen that the behavior of the SH wave deviates from the Gaussian beam propagation in the horizontal plane, which is the walk-off plane.

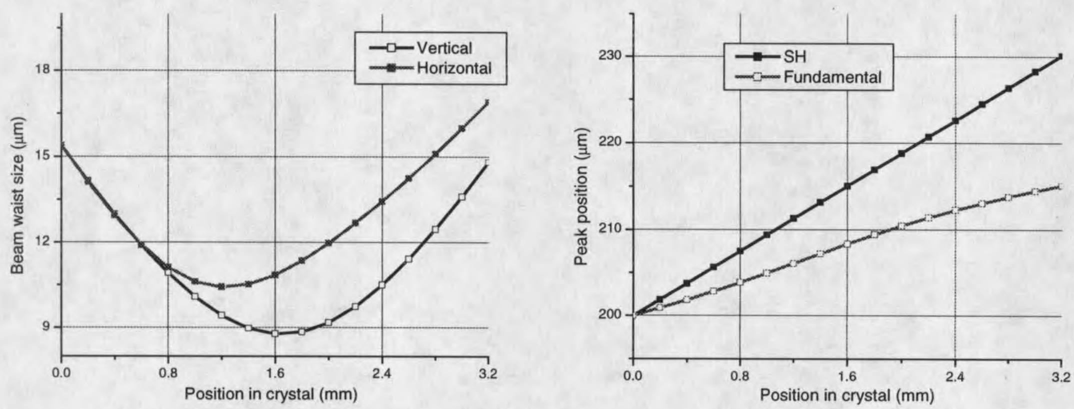

Figure-3.4 (a) The beam waists of the SH wave inside the crystal for the horizontal and the vertical directions; the walk-off is along the horizontal plane. (b) The peak positions of the fundamental and SH wave inside the crystal in the horizontal plane.

In Figure-3.4 (b), the peak positions of the fundamental and the SH wave in the crystal are plotted. The fundamental wave moves a distance of $30.18\ \mu m$ in the 3.2mm crystal length, and this is consistent with the calculated walk-off angle of $\rho = 0.0094$. This can also be used to check the accuracy of the simulation.

In the experiments, the optimum Δk is determined by finding the maximum SH power. Thus to make a comparison of the experiment with the calculation, the phase mismatching has to be considered. In Figure-3.5 (a), the optimum phase mismatch Δk is plotted with the input fundamental beam waist sizes for a crystal length of 3.2mm, and the beam waists are located at $l_w = 0, \frac{L_c}{4}, \frac{L_c}{2}, \frac{3L_c}{4}$, and L_c. As can be expected, at larger beam waists, the optimum phase mismatching Δk will go to zero, and a smaller beam waist will require a larger phase mismatching. When the beam waists deviate from the crystal center, the optimum Δk is still bigger than zero.

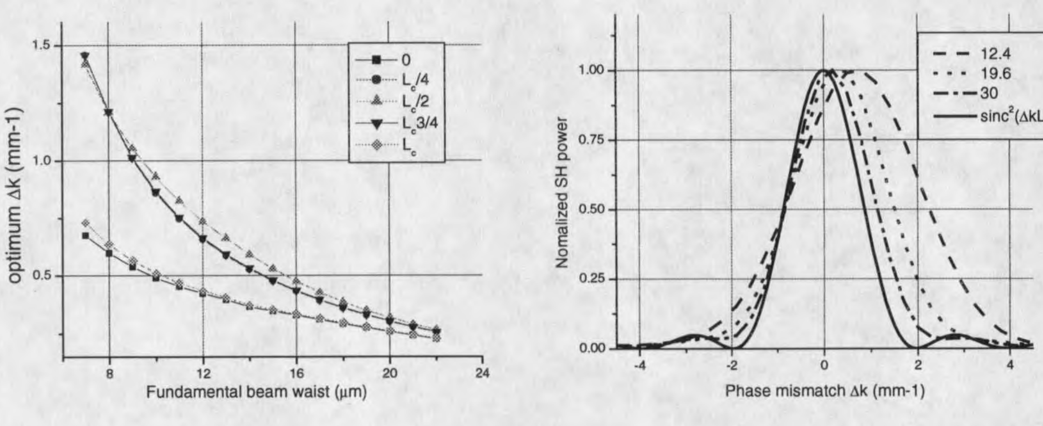

(a) (b)

Figure-3.5 (a) The optimum phase mismatching Δk vs. input beam waist for a 3.2mm crystal with the beam waist location at $l_w = 0, \frac{L_c}{4}, \frac{L_c}{2}, \frac{3L_c}{4}$, and L_c. (b) The normalized SH power with phase mismatching Δk for different fundamental beam waists.

In Figure-3.5 (b) the normalized SH power with Δk for different beam waist sizes is plotted, and the $\text{sinc}^2(\Delta k L_c/2)$ function of the plane wave model is also plotted for comparison. We can see that for smaller beam waists the shapes of the $P_{2\omega}-\Delta k$ curves are different from that of the $\text{sinc}^2(\Delta k L_c/2)$ function, and at large Δk the SH power goes to zero slowly instead of oscillating like the $\text{sinc}^2(\Delta k L_c/2)$ function. The bandwidth of Δk for the SHG with a focused Gaussian beam is also larger than that of the $\text{sinc}^2(\Delta k L_c/2)$ function. Thus the spectral, angular and temperature bandwidth will be larger than those predicted by the plane wave model. It is easy to show that for a fundamental beam with 12.4 μm waist size, those bandwidths will be 79% bigger, and for that with 19.6 μm waist size, 35% bigger, than those given by the plane wave model. When the beam waist is not located at the center of the crystal these numbers will be changed too.

In the experiments, to achieve the maximum conversion efficiency with a nonlinear crystal of a length L_c, we need to find the optimum beam waist size. In Figure-3.6, the SH power is plotted with the input fundamental beam waist sizes for a crystal length of 3.2mm, and the fundamental power is 3.6W. A maximum SH power is achieved when ω_0 =10.9 μm and the waist is at the center of the crystal, which is slightly bigger than the value of ω_0 =10.3 μm predicted by the Boyd-Kleinman theory. The optimum beam waist also depends on the waist location as shown in Figure-3.6. Also we can see that the location of the beam waist can greatly affect the conversion efficiency. Thus it is necessary to find the dependence of the SH powers on the beam waist location.

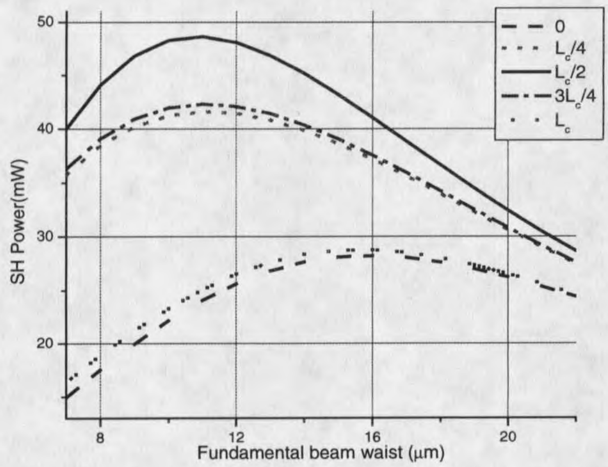

Figure-3.6 The SH power vs. input beam waist size. The crystal length is 3.2 mm, the beam waist location is at the center of the crystal, and the fundamental power is 3.6 W. A maximum SH power is achieved when ω_0 =10.9 μm.

In Figure-3.7, the SH power is plotted with the beam waist location for the waist sizes of 12.4 and 19.6 μm. As can be expected, the maximum SH power is achieved when the beam waist is at the center of the crystal.

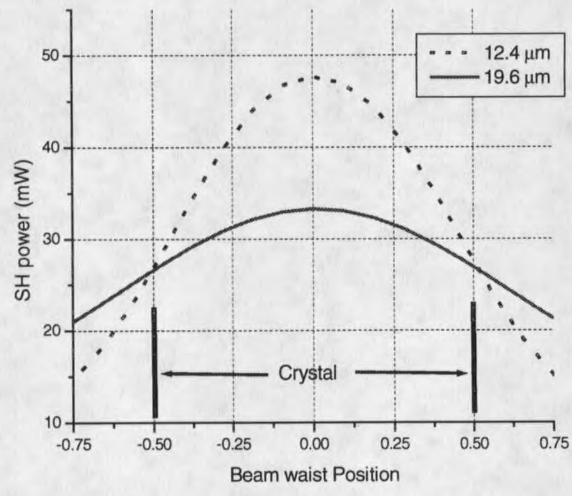

Figure-3.7 SH power vs. beam waist location of the fundamental wave for beam waist size of 12.4 and 19.6 μm

In the external resonant cavity, the beam waist location is determined by the position of the crystal inside the cavity, thus we need to find the SH power's dependence on the position of the crystal. According to Equation-2.11 in Chapter 2, the beam waist location from the center of the crystal is $x = \frac{t_2}{d_e}\Delta$, and for small incident angle ϕ, $x \approx n\Delta$. Thus for a 12.4 μm input beam waist, a positioning accuracy of better than 0.7 mm is required for a 3.2 mm long crystal to have a conversion efficiency within 50% of the peak value. From the above plot we can see that although the SH power of a 12.4 μm beam waist is about 43% higher than that of 19.6 μm, the SH power is very sensitive to the position of the crystal. This is one of the important factors that need to be considered when we design a SHG system.

<u>Beam profile and the beam quality of the SH wave</u>

Once the electromagnetic field at the output of the crystal surface $E_{out}^{2\omega}$ is known, the far field pattern, astigmatism and the beam propagation factor M^2 can be calculated. The far field pattern of the SH light can be calculated using the Fraunhofer's diffraction equation[6]:

$$U(x,y) = \frac{e^{ikz} e^{i\frac{k}{2z}(x^2+y^2)}}{i\lambda z} \int\int_{-\infty}^{+\infty} V(\xi,\eta) \exp\left[-i\frac{2\pi}{\lambda z}(x\xi + y\eta)\right] d\xi d\eta \qquad 3.14$$

where $U(x,y)$ is the far field distribution, $V(\xi,\mu)$ is the field distribution on the crystal output surface, and z is the distance between crystal surface and the observation plane. Thus the far field pattern is:

$$U^2(x,y) \propto \left|\tilde{e}_2^{\,out}(k_x,k_y)\right|^2 \qquad \text{with } k_x = \frac{2\pi x}{\lambda z}, k_y = \frac{2\pi y}{\lambda z} \qquad 3.15$$

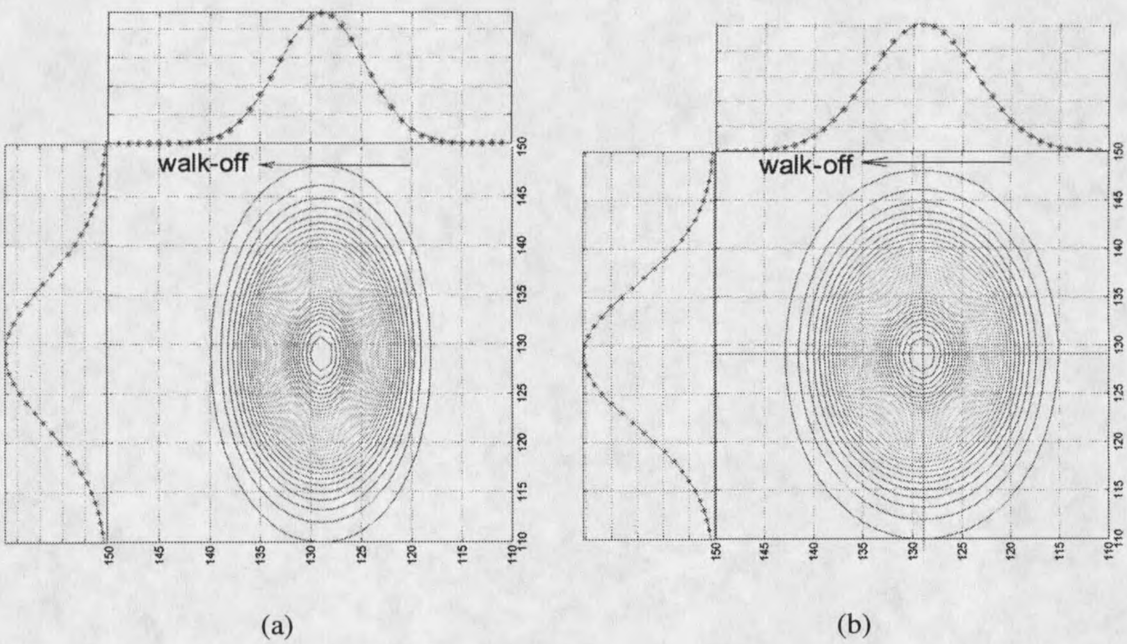

Figure-3.8 Far-field pattern of the SH wave. Because the walk-off direction is in the horizontal plane, inside the crystal the SH field will spread wider in the horizontal than in the vertical plane. Thus in the far field, the beam waist in the horizontal plane is shorter than that the vertical plane. (a) Beam waist ω_0 =12.4 μm . The ellipticity is 1:1.68, and the Gaussian fit for the horizontal plane is 98.3% (b) Beam waist ω_0 =19.6 μm . The ellipticity is 1:1.34, and the Gaussian fit for the horizontal plane is 99.5%.

In Figure-3.8, the far field patterns of the SH wave are plotted. The fundamental beam waists are 12.4 μm and 19.6 μm , located at the center of the crystal. We can see that because of the beam walk-off, even when the fundamental wave has a circular beam shape, the SH wave can have an elliptical beam shape. The fit coefficients of the Gaussian fittings are more than 98% in both cases. We also find that the location of the fundamental beam waist only slightly affects the ellipticity and the fitting of the far-field distribution. Thus the far-field distribution of the SH wave can be considered as a good Gaussian distribution.

To calculated the beam propagation factor M^2, we need to focus the beam, and measure the beam diameter at different positions including at the beam waist, then fit these data points to the Gaussian beam propagation equation[42]:

$$\omega(z) = \omega_0 \sqrt{1 + \frac{(z - z_d)^2}{z_0^2}} \qquad 3.16$$

with the Rayleigh range

$$z_0 = \frac{\pi \omega_0^2}{M^2 \cdot \lambda} \qquad 3.17$$

and M^2 is the beam propagation factor.

This process is simulated by the following procedure: Because the output properties of the SH wave is completely determined by the electromagnetic field at the crystal output surface $E_{out}^{2\omega}$, the field $E_{out}^{2\omega}$ can also be considered as generated in an isotropic medium with a refractive index of $n^{2\omega}$. The beam is then propagated from a beam waist with the effective waist sizes of $\omega_{0,x}^{EFF}$ and $\omega_{0,y}^{EFF}$ for the horizontal and the vertical plane, and the beam propagation factor M^2 can be calculated. The field $E_{out}^{2\omega}$ is back-propagated toward its beam waist. The electromagnetic field at different positions and the waists $\omega(z)$ for the horizontal and the vertical planes are then calculated. ω_0, M^2 and z_d are then calculated by fitting $\omega(z)$ to Equation-3.16.

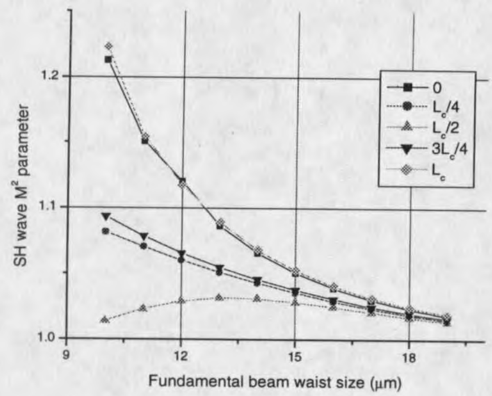

(a)

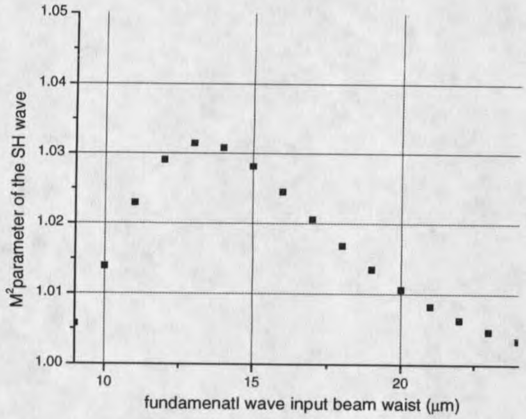

(b)

Figure-3.9 The propagation factor M^2 of the SH wave for different input beam waist sizes. (a) the beam waist locations are $l_w = 0, \frac{L_c}{4}, \frac{L_c}{2}, \frac{3L_c}{4}$ and L_c, (b) the beam waists are at the center of the crystal.

The M^2 parameters for the horizontal and the vertical planes are shown in Figure-3.9 for different beam waist sizes and beam waist locations. As can be expected, the M^2 parameters in the vertical plane are 1. If the beam waists are located at the center of the crystal, the M^2 parameters in the horizontal plane are only degraded slightly, the values are in the range between 1.0~1.04, the SH waves are basically close to perfect Gaussian beams. The M^2 parameters are more easily degraded by the deviation of the beam waist location form the center of the crystal, as can be seen from Figure-3.9 (a).

The effective beam waist sizes for the horizontal and the vertical direction are plotted for different input waist sizes in Figure-3.10 (a). We can see that the effective beam waist sizes in the walk-off plane are much bigger than those in non walk-off plane. This is consistent with the far-field pattern plotted in Figure-3.8, where the beam waist in the horizontal plane is shorter than that the vertical plane. From Figure-3.10 (b), we can see that when the beam waist is at the center of the crystal, only a slight astigmatism is generated.

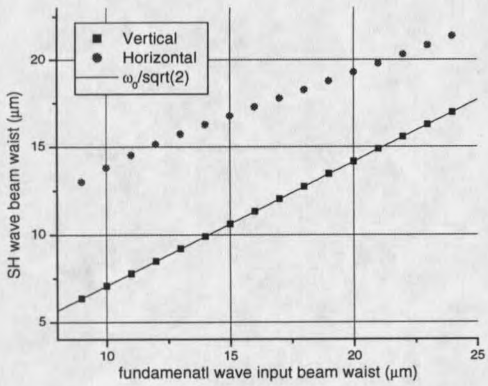

(a)

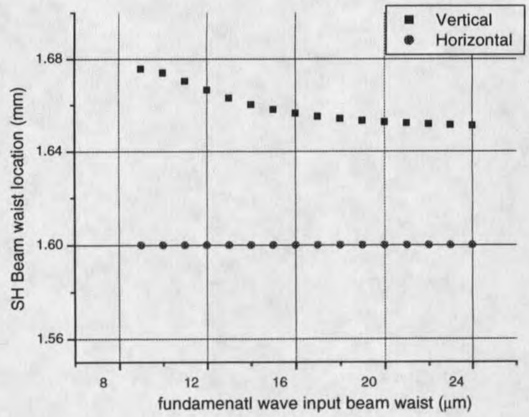

(b)

Figure-3.10 (a) The effective beam waist sizes of the SH wave in the horizontal and the vertical planes with the fundamental beam waist sizes. (b) The astigmatism of the SH wave.

The profiles of the SH beams at the focus are also good Gaussian profiles when the fundamental beam waists are at the center of the crystal. Only when the locations move away from the center of the crystal, are the profiles degraded. This can be observed from Figure-3.11 (a), where the beam profiles are plotted for a beam waist located at $l_w = \frac{3}{4} L_c$, for a beam waist of 12.4 and 19.6 μm, and the fit coefficients of the Gaussian fitting are 88.3% and 95% in the horizontal plane.

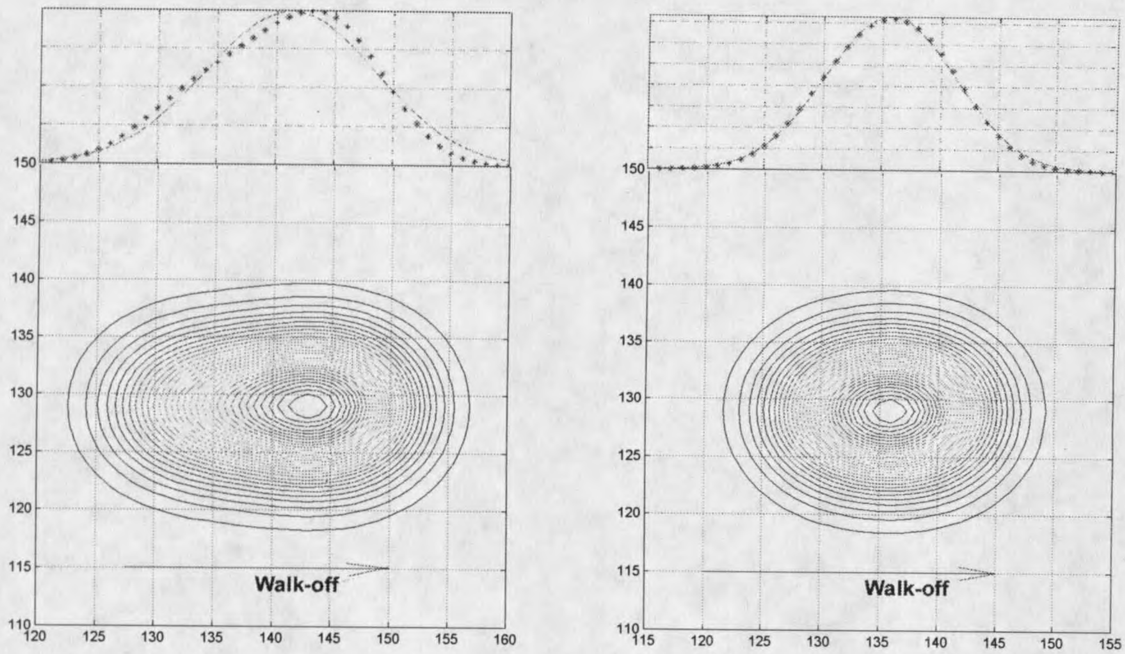

Figure-3.11 The profiles of the SH beams at the focus with the fundamental waist located at $l_w = \frac{3}{4} L_c$ (a) for fundamental beam waist of 12.4 μm and (b) 19.6 μm

Discussion and Conclusion

From the simulations we find that behavior of the SHG with focused Gaussian beams in a birefringent medium are much different from those predicted by the analysis with some effects being ignored. When designing a SHG system, we must be careful using the results from these analyses. The beam quality of the SH wave, which is a consideration for many applications, is not degraded when the beam waist is located at the center of the crystal, only the ellipticity is changed. The location of the beam waist, which is often ignored in many analyses, could seriously degrade the beam quality and reduce the conversion efficiency especially for tightly focused beams.

Though the beam depletion effect has been considered, the simulations we presented so far are in the low conversion efficiency region. At high conversion efficiency, the results can be much different.

CHAPTER 4

CONSTRUCTION OF A BLUE LIGHT SOURCE BY SHG

The initial motivation of our experiment came from the need to construct a blue light source in the 484nm-488nm region for spectroscopy. The requirements include: a few milliwatts of output power, low intensity and frequency noise, good frequency stability, diffraction-limited spatial mode, and a large mode-hop free scanning range of over 10GHz. Compact blue light sources are of great interest for a number of applications. Because the blue light has a shorter wavelength compared with red and infrared light, a smaller spot size can be achieved. Thus higher density in data storage and higher resolution in high-end printing can be reached. In color displays, red, green and blue are the basic colors, of which red can be generated by diode lasers at around 620nm and green by frequency doubled Nd:YAG lasers, but low cost stable blue lasers are still under development. In medical diagnostics, lasers at 488nm are the light sources used in the flow cytometer analysis. Semiconductor lasers operating at such wavelengths are the ideal choices because they could be efficient and have potentially low cost. However current blue-emitting Ga-N based diode lasers are limited in wavelength (390nm-420nm), power (<10mW) and lifetime. Frequency doubling an infrared diode laser provides a good alternative and offers several advantages to other types of light sources at this blue region. As discussed in the Chapter 1, these advantages include: high efficiency, high available power, large wavelength tuning range, good reliability, compactness, and low cost.

Experimental setup and apparatus

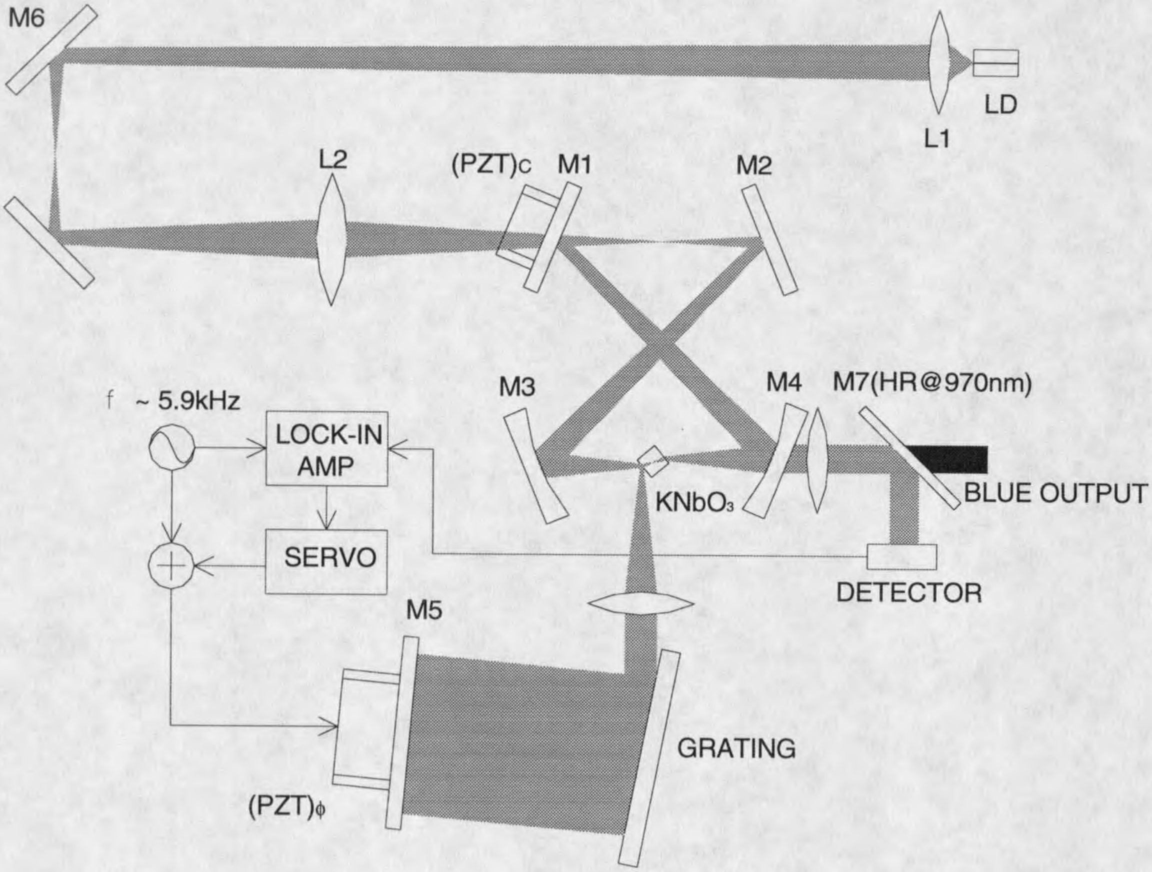

Figure-4.1 Experimental setup. The bow tie ring cavity is formed by M1, M2, M3 and M4. The reflection off the $KNbO_3$ crystal is reflected back by the grating-mirror (M5) to provide the feedback for single mode operation and frequency locking. LD, laser diode; L's, lenses; M's mirrors; PZT, piezoelectric transducer.

The experimental setup is shown in Figure-4.1. The fundamental light is provided by a commercial high power 970nm InGaAs Fabry-Perot diode laser (SDL-6530-J1) without any special preparation. The threshold current is 18mA, and the maximum output power is 200mW at a 250mA injection current.

The spectrum of the diode laser is shown in Figure-4.2 (a) for the diode laser with an injection current of 240mA.The FWHM of the main mode is about 1.3GHz measured using a Fabry-Perot interferometer with a free spectral range (FSR) of 38GHz and a finesse of 61 as shown in Figure-4.2 (b). The measured frequency tuning of the diode laser by current is 1.65GHz/mA. The emitting dimensions are 3 $\mu m \times 1$ μm. Because the spatial mode matching to the external cavity is important, the output beam waist and the astigmatism of the diode laser were carefully measured. The measured beam waists are 0.78 μm and 1.9 μm for the direction vertical to the junction and parallel to the junction, with an astigmatism of 6.7 μm. The direction of the polarization is along the junction, and the extinction ration ratio is 100:1 as specified by the manufacturer.

The doubling nonlinear crystal is a 3.2 mm long b-cut $KNbO_3$ crystal, which has a relatively large nonlinear coefficient (see Appendix C). Near 970nm, non-critical phase matching, which means the beam propagates along the principle axis and the temperature of the crystal is changed to meet the phase matching condition, requires cooling the crystal to about -16°C. Thus we chose to use critical phase matching, which means the angle of the crystal is changed to meet the phase matching condition. The angle of incidence on the crystal is about 40° at 25°C, and the walk-off angle ρ between the fundamental light and the generated blue is calculated to be 9.4 mrad. The effective nonlinear coefficient is d_{eff}=12.5pm/V.

The diode is placed so that the polarization of the output beam is in the horizontal plane. As discussed in chapter 2, we used two lenses, L1 (f =4.5mm 0.55 NA) and L2 (f =38.6mm) separated by 400mm to focus the output beam into the large beam waist and correct the astigmatism of the diode laser. By finely adjusting the position of the lens L1, we have a focus in both the vertical and horizontal direction located about 510 mm behind the second lens; the beam waist is 69 μm for the horizontal and 194 μm for the vertical directions, respectively.

The external cavity is a bow tie ring cavity, and the radius of the spherical mirrors is 25mm. The first plane mirror (M1) has a reflectance of 97% at 970nm, and all other three mirrors are high reflectors with reflectance greater than 99.3% at 970nm. The transmission loss of the SH output mirror M4 is measured to be 30% at 485nm. Of course a higher transmission is desired to reduce the SH loss. The $KNbO_3$ nonlinear crystal antireflection coated for 968-976nm is placed at the midpoint between the two spherical mirrors, where the smaller beam waist is located. The temperature of the crystal is stabilized to within 0.1K using a TEC.

The distance between the two spherical mirrors is 31.2mm, and the distance between the two spherical mirrors via the plane mirrors is 111mm. The incident angle on all four mirrors is 22.5°. Using Equations 2.6 and 2.7, we calculated that the large elliptical beam waist is 69 μm (horizontal) and 194 μm (vertical) between the plane mirrors for efficient mode matching the diode output, and a small circular beam waist of 19.6 μm inside the crystal. This 19.6 μm beam waist is bigger than the optimal beam waist size for a 3.2 mm long crystal, which is 10.9 μm from the simulation in Chapter 3. It is determined by the radius of the spherical mirrors as we can see from Equations 2.6 and 2.7. The total optical length of the ring cavity is 145mm, which gives a free spectral range (FSR) of 2.07GHz.

The reflectance of the coated $KNbO_3$ crystal surface was measured to be 0.48% at 40° incidence at 970nm. The absorption loss at 970nm inside the crystal is about 0.3%, estimated from the given values of the manufacture. Without the SHG, the power enhancement factor α and the finesse F of the cavity can be calculated using the equations:

$$\alpha = \frac{1-R_1}{\left(1-\sqrt{R_1(1-L)}\right)^2}$$

$$F = \frac{\pi[R_1(1-L)]^{1/4}}{1-[R_1(1-L)]^{1/2}} \qquad 4.1$$

where R_1 is the reflectance of the input mirror M1, and L describes all linear losses in the cavity exclusive of that of the input mirror. Using the above numbers, the calculated power enhancement of the cavity is about 36, and the finesse of the cavity is about 107. Thus the linewidth of the external cavity is 19.3MHz. Compared with the linewidth of the diode laser, which is1.3GHz, and the spectrum in Figure-4.2 (b), which has a small side mode suppression ratio of less than 10dB, we will have to significantly narrow the linewidth of the diode laser and make the diode laser operate in single mode to achieve efficient SHG.

Passive locking

In order to achieve stable fundamental build up inside the external cavity, the frequency of the diode laser has to be stabilized to the resonance of the external cavity. A passive locking method is applied in our experiment to lock the diode laser to the cavity resonance. Passive locking[43,44,45,46] sends back the transmission of an external cavity into the diode laser. Thus when the frequency of the diode laser is near the cavity resonance, it will automatically jump to the resonance and lock to this frequency. At the same time, the frequency noise can be greatly lowered, reducing the linewidth of the diode laser considerably. In the experiment, the reflectance from the first surface of the $KNbO_3$ crystal is collimated with a f =50mm lens. After reflecting off the grating-mirror (M5), it goes back into the cavity and is then fed back to the diode laser. The grating (1 inch long, 600 groove/mm) works in the Littman configuration with the third order light being reflected back with an efficiency of about 50%. Because our laser has a relatively wide spectral range and a side-mode suppression ratio of only about 10dB, this additional grating has to be used. Without using this grating feedback scheme, the counter propagating fundamental light inside the cavity created by the scattering from the crystal is fed back to the diode, causing the laser to operate multimode with chaotic behavior.

The feedback level to the diode laser can be calculated by measuring the backward leakage power after mirror M6, and the coupling efficiency back to the diode laser is estimated to be about 50%. Thus the feedback into the diode laser is on the order of 10^{-3}. Generally to achieve optical locking, only a small amount of feedback is necessary, for example, 10^{-6} of the output power. In our experiment a higher feedback level is necessary primarily for two reasons: First, the feedback from the crystal surface is estimated to be on the order of 10^{-4}, so the grating feedback must be significantly higher to suppress this feedback. Second, the locking range depends on the feedback power ratio[47]; that is, the higher the feedback level, the larger the locking range. Thus with higher feedback, we can achieve optical locking without fine control of the external cavity length. We only need to adjust the angle of the mirror M5 to make sure the feedback from the grating (FWHM ~6.8GHz) falls on one of the diode longitudinal modes.

With the feedback from the grating dominating other feedback, the diode laser operates in a single mode. The spectrum with feedback is also shown in Figure-4.2(a). We can see that the spectrum narrows and the side mode suppression ratio increases to greater than 40 dB. Because optical locking is sensitive to the phase of the feedback light, external perturbations will cause instability of the diode laser. Secondly, because the spacing of the external cavity resonances is 2GHz and the FWHM of the grating is 6.8GHz, external perturbations can also cause the laser frequency to hop between different cavity resonances. For long-term stable operation and to be able to scan the laser frequency, the optical path length between the diode laser and the feedback mirror (M5) has to be actively controlled. To control the phase ϕ of the feedback phase, a piezoelectric transducer, labeled (PZT)ϕ, is mounted on mirror M5. Modulating the path length at 5.9kHz and monitoring the transmitted fundamental light by a lock-in amplifier generates the error signal. This error signal is fed back to the (PZT)ϕ via a servo amplifier for active control of the feedback phase.

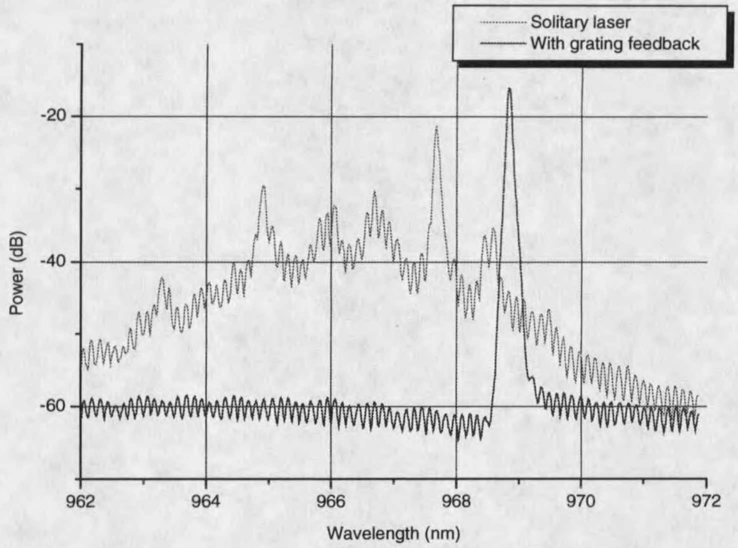

(a)

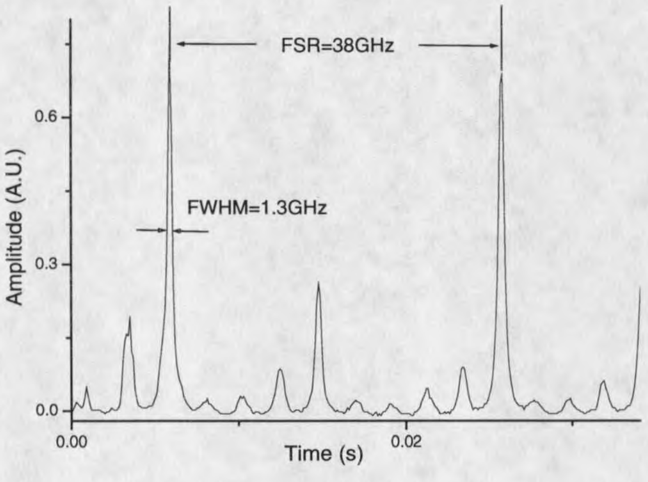

(b)

Figure-4.2 The spectrum of the laser diode. (a) Measured using an optical spectrum analyzer with a resolution bandwidth is 0.08nm. Note that with grating feedback the spectrum narrows and the side mode suppression ratio increases to greater than 40 dB. The peak wavelength can be tuned by adjusting the angle of mirror M5. (b) The spectrum of the laser diode without feedback measured using a scanning Fabry-Perot interferometer with a free spectral range (FSR) of 38GHz and a Finesse of 61.

Experimental results

As we have discussed in Chapter 2, to achieve efficient mode matching between the diode laser and the external build-up ring cavity, the beam waist sizes of the focused diode laser output beam must be the same as those of the larger elliptical beam waist of the ring cavity in both the vertical and horizontal planes. To verify this, we slightly misalign the cavity, so that the individual transmission of the beam inside the cavity through mirror M2 is separated. We observe the beam profiles of the multiple transmissions using a charge-coupled detector (CCD) camera. By careful adjustment of the position of lens L1, the beam profiles will closely resemble each other, an indication of good mode matching. The beam profile of a portion of the transmission is shown in Figure-4.3 (a). The beam profile of the transmission when the cavity is aligned is also shown in Fighre-3 (b), and for comparison the beam profile of first transmission is also shown. The mode-matching factor m is calculated using[48]:

$$m = \left(\frac{2\omega_x \omega_{cx}}{\omega_x^2 + \omega_{cx}^2} \cdot \frac{2\omega_y \omega_{cy}}{\omega_y^2 + \omega_{cy}^2} \right)^2 \qquad 4.2$$

where ω_x, ω_y , ω_{cx} and ω_{cy} are the beam waist sizes of the Gaussian fit for the first transmission and the cavity transmission in the horizontal and vertical directions measured in Figure-4.3 (b). The calculated mode-matching factor is about 80%. We didn't achieve a higher mode matching because of the error in the measured beam waist size of the diode laser, and its dependence on temperature and injection current.

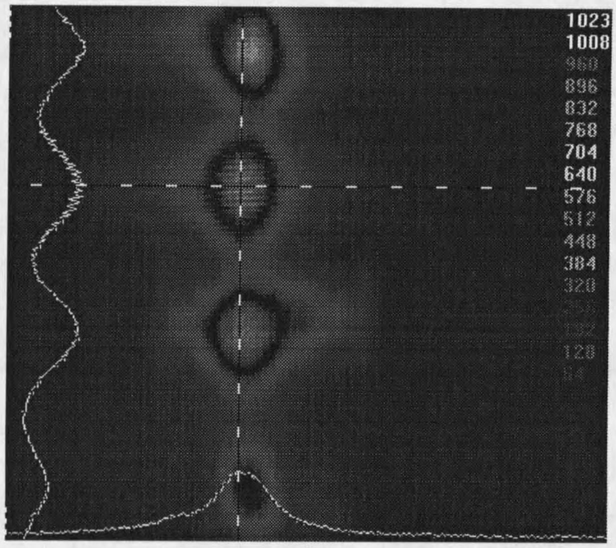

(a)

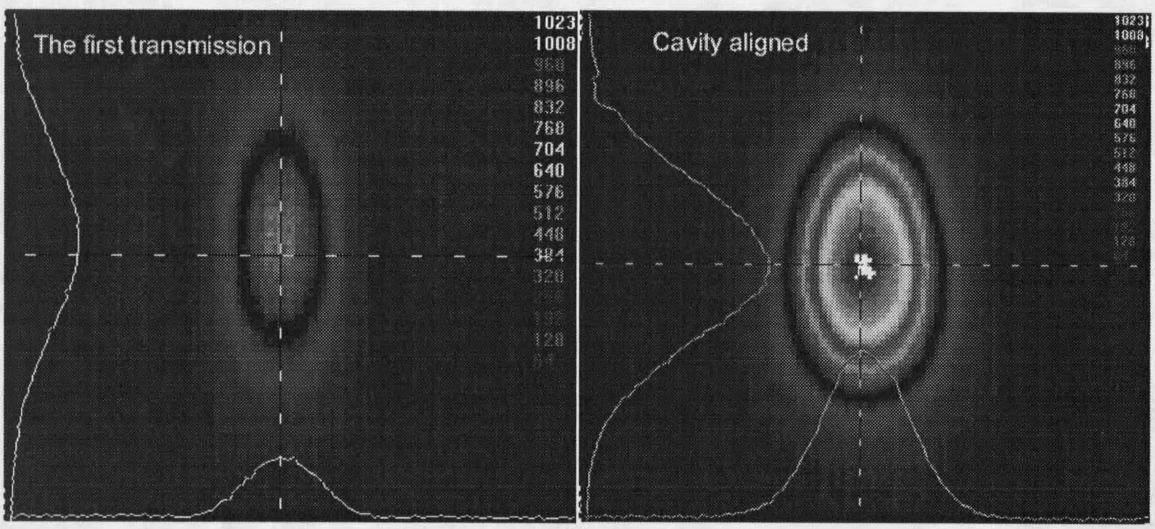

(b)

Figure-4.3 (a) The beam profile of a portion of the transmissions when the cavity is slightly misaligned. (b)The beam profile of the transmission when the cavity is aligned. For comparison the beam profile of first transmission is also plotted.

Other factors affecting the mode matching are the positioning of the lenses and the cavity, misalignment of the cavity, and that the output beam of the diode laser is not perfectly Gaussian. Still compared with other experiments that achieved a mode matching factor of 60%-70%[49,50], our setup improves the mode matching with simplicity. A large mode-matching factor is important for high conversion efficiency as well as for the stability of the system, since the stability of the diode laser with feedback depends greatly on the waveform of the feedback light.[51]

With 192mW of diode output power, the available power before the cavity is about 183mW. On resonance, the circulating fundamental power inside the cavity is about 3.5W. This is calculated by measuring the cavity leakage through mirror M2. Thus the enhancement of the fundamental light is about 24. About 40% of the infrared input power is reflected at input mirror M1 due to reflectivity mismatch. The enhancement could be further improved by selecting the optimum transmission T_1 of the input coupler by using equation[52]:

$$T_1 = L/2 + \sqrt{L^2/4 + E_{NL} m P_1} \qquad 4.3$$

where L describes all linear losses in the cavity exclusive of T_1, $E_{NL} = P_2 / P_1^2$ is the single pass nonlinear conversion efficiency, m is the mode matching factor, and P_1 is the fundamental input power. This optimization comes from matching the loss in the cavity and the nonlinear conversion to the reflectivity needed for maximum coupling to the cavity.

The maximum blue output is 18.45 mW measured after M6. Considering reflection of the crystal, the spherical mirror and the high reflector M6, we estimate 35% of the blue light generated is lost giving 28.3mW of blue generated. The calculated blue light generated with the pump power inside the cavity is plotted in Figure-4.5. The simple quadratic fit gives us a nonlinear conversion efficiency E_{NL}=0.23%/W. Using the simulation in Chapter 3, we obtained a theoretical nonlinear conversion efficiency of 0.26%/W. This discrepancy is caused mainly by inaccurate estimation the loss by the reflection of mirrors (M6 and M4) and the $KNbO_3$ crystal surface. The second reason is the loss of the SH wave inside the crystal is not considered in the numerical simulation. The quality of the nonlinear crystal can also differ from the ideal one, thus the conversion efficiency can be lowered.

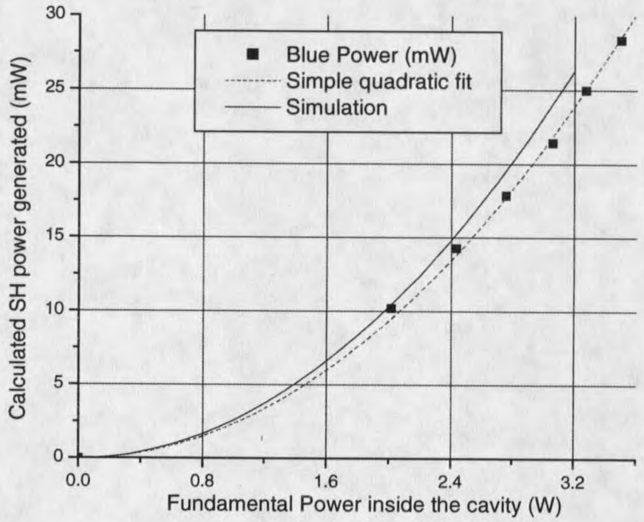

Figure-4.4 The calculated blue light generated with the pump power inside the cavity. The theoretical fit is the simple quadratic growth expected from SHG theory for low conversion efficiency. The solid line is the result from the simulation.

The system is mounted on a thick aluminum plate and covered with an aluminum box to prevent airflow to improve the stability. The blue output power over a 30-minute time period is shown in Figure-4.5, with a peak-to-peak fluctuation of less than 0.02dB. For the longer-term stability, the fluctuation increases due to the temperature of the room, which causes the length of the ring cavity to change. When the change is too big for the

(PZT) ϕ to correct, a mode hop can occur, and the continuous operation is interrupted. Because the frequency response bandwidth of the (PZT) ϕ is small, mechanic shock can also disrupt stable operation.

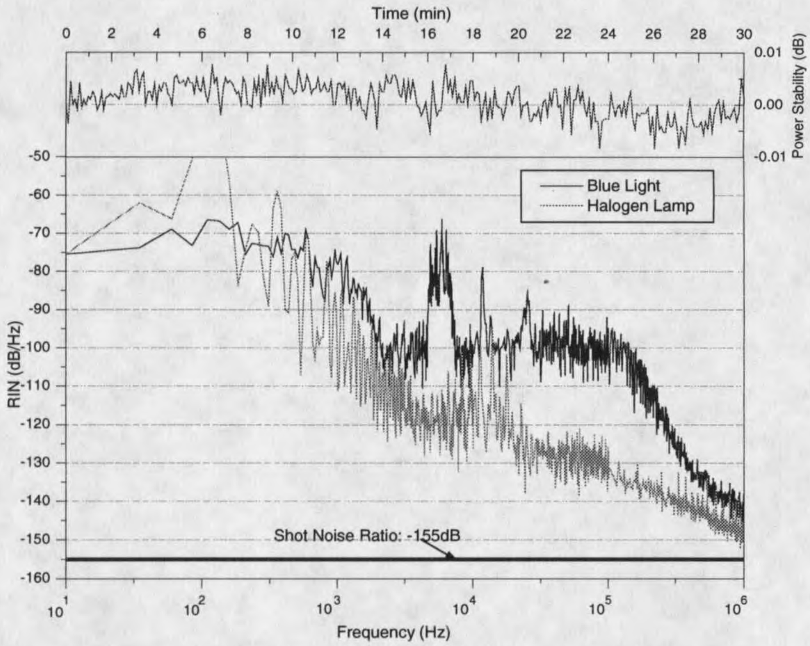

Figure-4.5 The output blue light power fluctuation for 30 minutes and the relative intensity noise (RIN) of the blue light and the RIN of a red-filtered halogen lamp. The noise of the red-filtered halogen lamp above shot noise level is mainly caused by $1/f$ noise.

To measure the intensity noise, the blue output light is focused on a detector (New Focus 1621); the photocurrent noise is amplified by 40dB and measured by a spectrum analyzer. With 4.5mW of blue light, the detector current is 1.01mA. The noise of a red-filtered halogen lamp (a source of classical light) is also measured by the detector with a 1.01mA photocurrent. The relative intensity noise (RIN) of the blue light shown in Figure-4.5 is calculated using:

$$RIN = S(f) - 10\log(I_{DC}{}^2 Z_0) - 40 \qquad 4.4$$

where $S(f)$ is the measured power spectral density of the photocurrent by the spectrum analyzer, and Z_0 is the impedance of the spectrum analyzer. The shot noise ratio calculated is -155dB using equation:

$$RIN_{shot} = 10\log_{10}\frac{2q}{I_{DC}} \qquad 4.5$$

where q is the electron charge, I_{DC} is the photocurrent.

The highest peak of the blue light noise is the modulation frequency at 5.9kHz. At high frequency the blue light intensity noise is about 10dB above the shot noise level. The intensity noise is sensitive to the diode operating current. When the diode laser current deviates from the optimum value by about 0.3mA, the diode laser will not lock to the exact peak of the cavity resonance, and we observe a much higher noise at the modulation frequency and an increased low frequency noise. As the current deviation increases, the system will completely lose stable locking, and the diode laser operation is multimode with chaotic behavior.

To measure the spatial quality of the output blue light, the output blue light is focused with a lens ($f = 123\,mm$) that is placed $140\,mm$ behind the center of the crystal to generate a larger beam focus (~200 μm). The beam intensity profile is measured with a beam profiler, and the beam waists of the horizontal and vertical plane with change of axial position z, are plotted in Figure-4.5 (a). The data is then fitted with the Gaussian beam propagation equation 3.16.

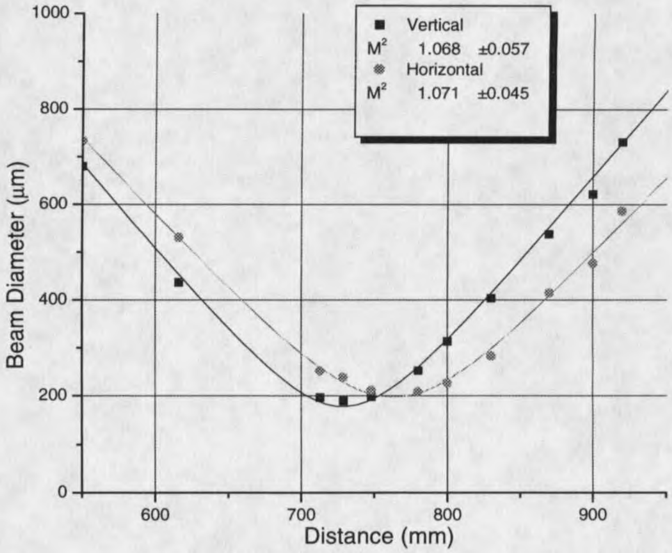

(a)

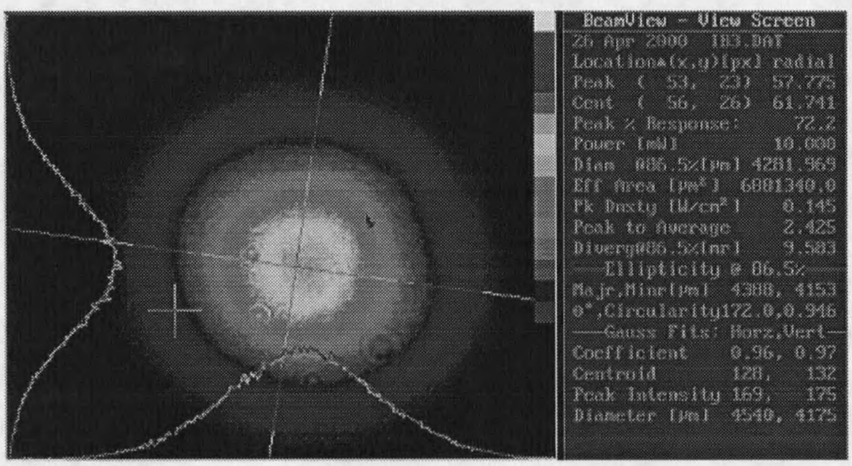

(b)

Figure-4.6 (a) Beam diameters of the horizontal and vertical plane with change of axial position z, the solid lines are least-square fit. The measured beam quality parameter M^2 is 1.071 and 1.068 for horizontal and vertical plane. (b) Beam profile of the output blue light at some arbitrary distance. The Gaussian fit for the horizontal and vertical plane is 97% and 96%.

The result of the fitting is also plotted in Figure-4.6 (a), and the beam waist is $98.7 \pm 4.7\ \mu m$ and $88.9 \pm 5.0\ \mu m$ for horizontal and vertical respectively, with an astigmatism of $40.2\,mm$. This slight ellipticity is expected from the simulation in Chapter 3, which the walk-off effect causes the effective beam waist in the horizontal plane to be larger than that in the vertical plane. The measured beam quality parameter M^2 is 1.07 ± 0.05 and 1.07 ± 0.06 for the horizontal and the vertical plane. Thus the output blue light is a near diffraction limited Gaussian TEM_{00} mode. In Figure-4.6 (b), the captured beam profile of the output blue light at some arbitrary distance is shown, and this is the far-field pattern. The fitting coefficient of the Gaussian fit for the horizontal and vertical plane is 97% and 96%, and the ellipticity is 1:1.12. Compared with the simulations in Chapter 3, the fitting coefficient of the Gaussian fit and the beam quality parameter M^2 are close to the simulation result.

To measure the frequency noise of the blue light, we use an F-P interferometer as an optical frequency discriminator to convert the FM noise into AM noise, and then measured with a photo detector and a spectrum analyzer. The interferometer has a free spectral range (FSR) of 1.5GHz and a finesse of 44. The single-sided frequency noise power spectrum $S_{FM}(f)$ is shown in Figure-4.7 (a). The highest peak is the modulation frequency of 5.9kHz; the peaks around 1kHz are the acoustic and mechanical vibrations. The linewidth of the blue light can be found by calculating the intensity spectrum $I(\nu)$ numerically, using the following equation[53]

$$\begin{aligned} I(\nu) &= 4 \cdot \mathrm{Re} \int_0^\infty d\tau \exp[i2\pi(\nu_0 - \nu)\tau] \\ &\times \exp[-2(\pi\tau)^2 \int_0^\infty S_{FM}(f) \frac{\sin^2(\pi f \tau)}{(\pi f \tau)^2} df] \end{aligned} \qquad 4.6$$

where ν_0 is the laser frequency.

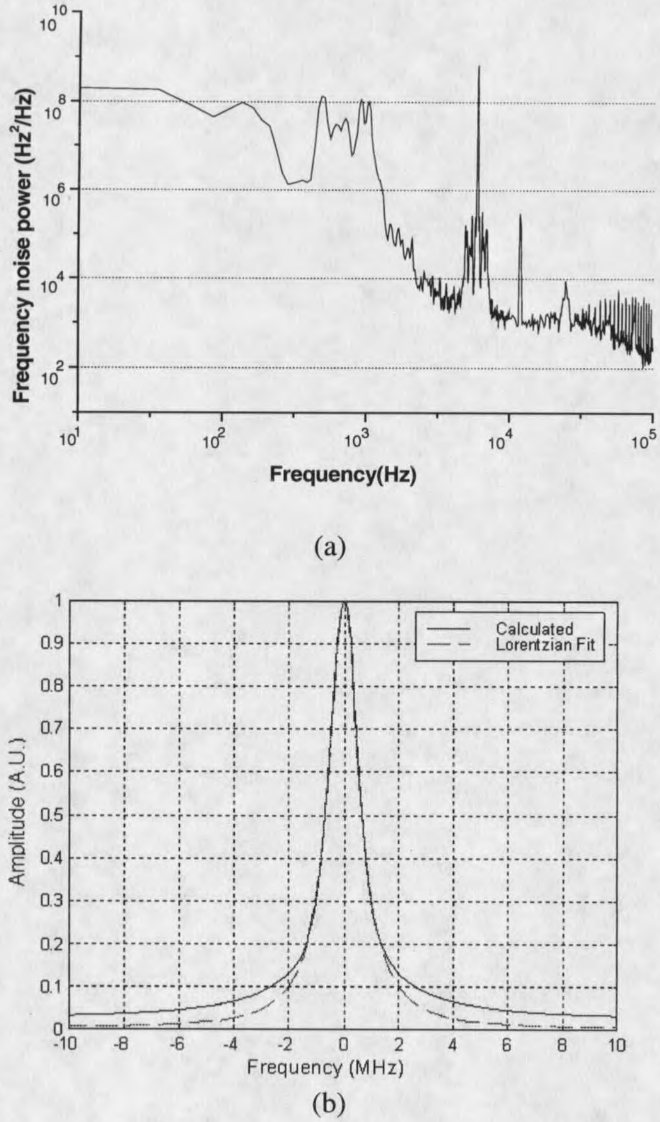

Figure-4.7 The single-sided frequency noise power spectrum of the blue light. The highest peak is the modulation frequency at 5.9kHz.Calculated field spectrum of the blue light, and the resulting linewidth is 1.25MHz. The dashed line is Lorentzian fit.

The calculated intensity spectrum is shown in Figure-4.7 (b), and the resulting linewidth is 1.25MHz. The fundamental light with feedback should have the similar linewidth. This linewidth is considerably narrower than that of the original laser. This gives a linewidth reduction factor on the order of 10^3. Thus this cavity and feedback can be used to reduce the laser linewidth and suppress the frequency noise.

To control the cavity length, a piezoelectric transducer, which we labeled $(PZT)_C$ is attached the cavity mirror M1. Thus by continuously changing the cavity length, we can tune the resonance frequency of the cavity. It is easy to show the change of the resonance frequency $d\nu$ of the ring cavity by change of the length dl is given by:

$$d\nu = -\frac{FSR}{\lambda} dl \tag{4.7}$$

To achieve a larger continuous frequency scanning range, the resonance frequency of the cavity, the feedback phase and the injection current of the diode laser need to be changed synchronously. This is done by finding the exact ratio of the applied voltage on $(PZT)_C$, $(PZT)\,\phi$ and the diode modulation.

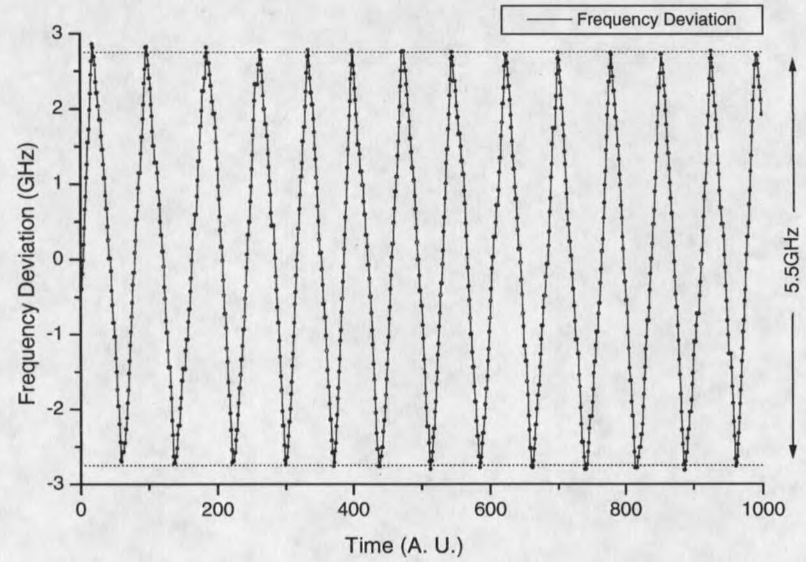

Figure-4.8 Measured frequency ramping of the fundament light by a wavemeter. The scanning range is about 5.5GHz, corresponding to 11GHz in blue.

We apply a sawtooth voltage across the $(PZT)_C$, and the frequency of the fundamental light is monitored by a wavemeter (Burleigh WA-1500). The frequency change with time is shown in Figure-4.8, and we can see that the scanning range is about 5.5GHz, corresponding to 11GHz for the blue output. The output power of the blue light changes slightly, because of the large acceptance bandwidth of the critical phase matched nonlinear generation (about 60GHz for 3.2mm long crystal).

The second experiment

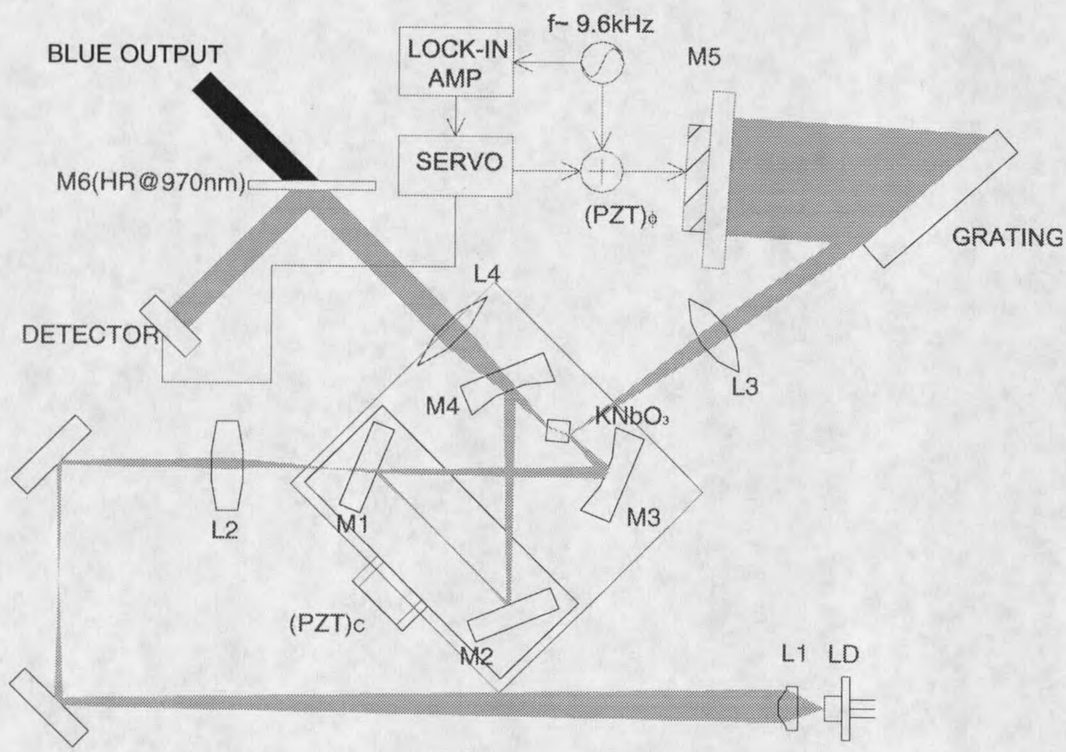

Figure-4.9 The setup for the second experiment.

From the simulation in Chapter 3, we find that the optimum beam waist is 10.9 μm for the 3.2mm long $KNbO_3$ crystal. Thus a second ring cavity was built with the radius of the concave mirrors being R =15mm. The input mirror M1 has a reflectance of 98% at 970nm, and all other three mirrors are high reflectors with reflectance greater than 99.9% at 970nm. The distance between the two spherical mirrors is 18mm, and the distance between the two spherical mirrors via the plane mirrors is 89.5mm. The incident angle on all four mirrors is still 22.5^{o}.The calculated beam waist inside the crystal is 12.4 μm , this will give us a SH power of 47.6 mW calculated from Chapter 3 if the enhancement remains the same. The setup is similar to the first experiment, and is shown in Figure-4.9. The maximum fundamental power inside the cavity is 3.6mW, and the maximum blue light measured after the high reflector M6 is 14mW. The far-field beam profile is shown in Figure-4.10. The ellipticity is 1.80:1, which is close to the simulation in Chapter 3. The transmission loss through M4 is about 40%, thus the blue light generated inside the cavity is about 28mW. This is about 42% less than that predicted by the simulation.

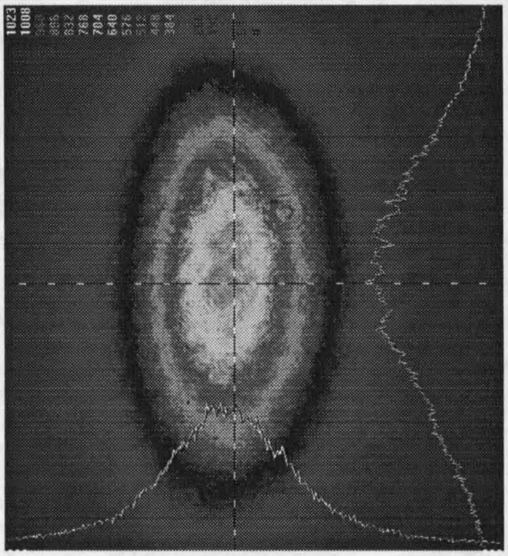

Figure-4.10 Far-field beam profile of the blue light. The ellipticity is measured to be 1:1.80.

To find out the reason, we took a photograph of the cavity with the beam trace of the fundamental light when the cavity is best aligned. Then the photo is overlapped with the designing AutoCAD plot, as shown in Figure-4.11. It is easily seen that the real beam path does not follow the designed path, which can be caused by the machining error of the cavity and positioning error of the optics. Thus the distance between the two spherical mirrors is not the desired length L, and the angle on the spherical mirrors is slightly different from the desired θ. Consequently the mode matching between the diode laser and the ring cavity can be degraded, and the smaller beam waist size inside the cavity is not what we have expected. More importantly, because the beam path is not what we have designed, the crystal is not at the midpoint between the two spherical mirrors along the real beam path, and the beam waist is not at the center of the crystal. As discussed in Chapter 3, the SH power with a small fundamental beam waist is easily degraded by this deviation of the beam waist location from the center of the crystal. Measured from the photo, the crystal is about 0.4mm off the midpoint between the two spherical mirrors along the beam path. Using the equation 2.13 and the simulation in Chapter 3, the calculated SH power is about 35mW.

In this second experiment, we use smaller 1/2 inch mirrors instead of 1 inch mirrors compared with the first cavity, and the overall size of the second cavity is about half of the first one. Thus at least twice the machining tolerance is required. For higher SH power, we need to increase the enhancement of the cavity, which is about 25. The loss of the fundamental light by the crystal (surface reflection and absorption, total about 1.3%) is a big factor limiting the enhancement and need to be reduced. We also need to reduce the reflection of the SH light by mirror M4, which causes more than 30% loss in both experiments.

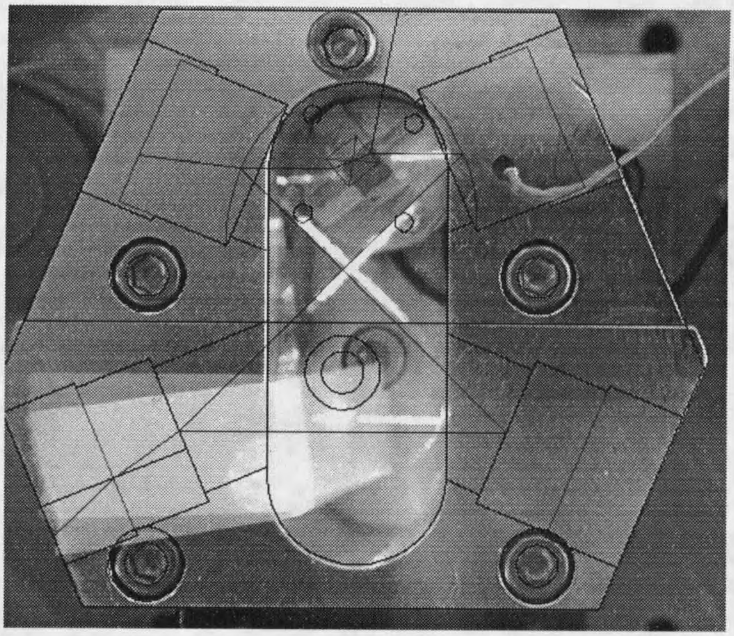

Figure-4.11 The real beam path and the designed beam path. Because of the machining and positioning error, the beam path when the cavity is best aligned can differ from the design.

CHAPTER 5

SUMMARY

In this thesis, we describe a simple scheme for development of a low noise CW blue light source by efficiently frequency doubling a Fabry-Perot diode laser. The optical-optical conversion efficiency is 9.6%. The blue light has low intensity noise, narrow linewidth and excellent spatial quality. The good mode matching between the diode laser and the external cavity is important to the conversion efficiency as well as to the low noise. Using curved mirrors with a smaller radius in the external ring cavity to decrease the beam waist size can improve the conversion efficiency, but at the same time higher mechanical precision is required, especially the positioning of the nonlinear crystal. From the numerical simulation of the SHG by the Fourier space method, we find that the positioning of the nonlinear crystal is the one critical factor for the conversion efficiency and the quality of the SH beam. Higher conversion efficiency can be achieved if the enhancement of the cavity is increased by reducing the loss in the cavity.

REFERENCES

[1] Amnon Yariv, "Quantum Electronics", 3rd edition, (John Wiley and Sons, New York, 1989)

[2] Robert W. Boyd, "Nonlinear Optics", (Academic Press, 1992)

[3] J. A. Armstrong, N. Bloembergen, J. Ducuing, and P. S. Pershan, "Interactions between light waves in a nonlinear dielectric," Phys. Rev. **127**, 1918 (1962).

[4] Gregory David Miller, "PERIODICALLY POLED LITHIUM NIOBATE: MODELING, FABRICATION, ANDNONLINEAR-OPTICAL PERFORMANCE", Ph.D. thesis

[5] P.A. Franken, A. E. Hill, C. W. Peters, and G. Weinreich, "Generation of optical harmonics", *Phys. Rev. Letters* **7**, 118 (1961)

[6] Y. Hirano, N. Pavel, S. Yamamoto, Y. Koyata, T. Tajime, "100-W, 100-h external green generation with Nd:YAG rod master-oscillator power-amplifier system", Opt. Comm. **184,** 231-236 (2000)

[7] Klaus Schneider, Sephan Schiller, and Jurgen Mlynek, "1.1W single frequency 532-nm radiation by second-harmonic generation of a miniature Nd:YAG ring laser', Opt. Lett. **21** 1999-2001 (1996)

[8] W. J. Kozlovsky and W. Lenth, "Generation of 41mW of blue radiation by frequency doubling of a GaAlAs diode laser", Appl. Phys. Lett. **56**, 2291-2292 (1990)

[9] D. Woll, B. Beier, K.-J. Boller, and Wallenstein, "1W of blue 465-nm radiation generated by frequency doubling of the output of a high-power diode laser in critically phase-matched LiB_3O_5", Opt. Lett. **24**, 691-693 (1999)

[10] B. Dahmani, L. Hollberg and R. Drullinger, "Frequency stabilization of semiconductor lasers by resonant optical feedback", Opt. Lett., **12**, 876-878 (1987)

[11] X. G. Sun, G. W. Switzer and J. L. Carlsten, "Blue light generation in an external ring cavity using both cavity and grating feedback", *Applied Physics Letters*, 76, 955-957 (2000)

[12] X. G. Sun, and J. L. Carlsten, "Low noise blue laser with large frequency scanning range by frequency doubling a diode laser", *Journal of the Optical Society of America* B, 18, March (2001).

[13] M. Bode, I. Freitag, a. Tunnerman, and H. Welling, "Frequency tunable 500-mW continuous-wave all-silid-state single-frequency source in the blue spectral region", Opt. Lett. **22**, 1220-1222 (1997)

[14]R. Paschotta, P. Kurz, R. Henking, S. schiller, and J. Mlynek, "82% Efficient continuous-wave frequency doubling of 1.06 μm with monolithic $MgO:LiNbO_3$ resonator", Opt. Lett. **19**, 1325-1327 (1994)

[15] E. S. Polzik and H. J. Kimble, "Frequency doubling with KNbO3 in an external cavity", Opt. Lett. **16**, 1400-1402 (1991)

[16] Z. Y. Ou, S. F. Pereira, E. S. Polzik, and H. J. Kimble, "85% efficiency for CW frequency doubling from 1.08 to 0.54 μm", Opt. Lett. **17**, 640-642 (1992)

[17] K. Kondo, M. Oka, H. Wada, T. Fukui, N. Umezu, K. Tatsuki, and S. Kubota, "Demonstration of long-term reliability of a 266-nm, continuous-wave, frequency-quadrupled solid-state laser using β-BaB_2O_4", Opt. Lett. **23**, 195-197 (1998)

[18] G. D. Miller, R. G. Batchko, W. M. Tulloch, D. R. Weise, M. M. Fejer, and R. L. Byer, "42%-efficient single-pass cw second-harmonic generation in periodically poled lithium niobate", Opt. Lett. **22**, 1834-1836 (1997)

[19] O. S. Brozek, V. Quetschke, A. Wicht, K. Danzmann, "Highly efficient cw frequency doubling of 854 nm GaAlAs diode laser in an external ring cavity", Opt. Commun. **146**, 141-146 (1998)

[20] W.J. Kozlovsky, W. P. Risk, W. Lenth, B. G. Kim, G. L. Bona, H. Jaeckel, D. J. Webb, "Blue light generation by resonator-enhanced frequency doubling of an extended-cavity diode laser", Appl. Phys. Lett. **65**, 525-527(1994)

[21] J. D. Bhawalkar,Y. Mao, ,H. Po,, A. K. Goyal, P., Gavrilovic, Y. Conturie, and S. Singh, "High-power 390-nm laser source based on efficient frequency doubling of a tapered diode laser in an external resonant cavity", Opt. Lett. **24**, 823-825 (1999)

[22] B. Beier, D. Woll, M. Scheidt, K.-J. Boller, and R. Wallenstein, "Second harmonic generation of the output of an AlGaAs diode oscillator amplifier system in critically phase matched LiB3O5 and β-BaB2O4", Appl. Phys. Lett. **71**, 315-316 (1997)

[23] C. Zimmerman, V. Vuletic, A. Hemmerich, and T. W. Hansch, "All solid state laser source for tunable and ultraviolet radiation", Appl. Phys. Lett. **66**, 2318-2320 (1995)

[24] Y. Hadjar, F. Ducos, and O. Acef," Stable 120-mW green output tunable over 2 THz by a second-harmonic generation process in a KTP crystal at room temperature", Opt. Lett **25**, 1367-1369 (2000)

[25] A. Hemmerich, D. H. McIntyre, C Zimmermann, and T. W. Hanch, " Second-harmonic generation and optical stabilization of a diode laser in an external ring resonator", Opt. Lett **15**, 372-274 (1990)

[26] Anish K. Goyal, Jayant D. Bhawalkar, Yves Conturie, Paul Gavrilovic, Yalan Mao, Hong Po, and John Guerra, "High beam quality of ultraviolet radiation generated through resonant enhanced frequency doubling of a diode laser", J. Opt. Soc. Am. B, **16**, 2207-2216 (1999)

[27] G.D. Boyd and D.A. Kleinman, , "Parametric interaction of focused Gaussian light beam," J. Appl. Phys. **39**, 3597- (1968)

[28] A. E. Siegman, Lasers(University Science, Mill Valley, Calif.,1986)

[29] H. Hogelink and T. Li, "Laser beams and resonators", Proc. IEEE, **Vol. 54**, 1312-1329 (1966)

[30] Herwig W. Kogelnik, "Astigmatically compensated cavities for CW dye lasers," IEEE J. Quantum Electron., Vol. **QE-8**, 373-379 (1972)

[31] A. E. Siegman, Lasers(University Science, Mill Valley, Calif.,1986)

[32] D. C. Hanna, "Astigmatic Gaussian beams produced by axially asymmetric laser cavities," IEEE J. Quantum Electron., Vol. **QE-5,** 483-488 (1969)

[33] G.D. Boyd and D.A. Kleinman, "Parametric interaction of focused Gaussian light beam", J. Appl. Phys. **39**, 3597-3639 (1968)

[34] P. Pliszka and P. P. Banerjee, ''Nonlinear transverse effects in second-harmonic generation,'' J. Opt. Soc. Am. B **10**, 1810–1819 (1993).

[35] M. A. Dreger and J. K. McIver, ''Second-harmonic generation in a nonlinear, anisotropic medium with diffraction and depletion,'' J. Opt. Soc. Am. B **7**, 776–784 (1990).

[36] S. C. Sheng and A. E. Siegman, ''Nonlinear-optical calculations using fast-transform methods: second-harmonic generation with depletion and diffraction,'' Phys. Rev. A **21**,599–606 (1980).

[37] Gunnar Arisholm, "General numerical methods for simulating second-order nonlinear interactions in birefringent media", J. Opt. Soc. Am. B, **10**, 1543-2549 (1997)

[38] Joseph W. Goodman, "Introduction to Fourier Optics", 2nd Edition, The McGraw-Hill companies, Inc. 1996

[39] Willam H. Press, Saul A. Teukolsky, Willam T. Vetterling, and Brian P. Flannery, "Numerical Recipes in FORTRAN—The art of scientific computation", 2nd Edition, Cambridge Univ. Press 1992

[40] J. A. Armstrong, N. Bloembergen, J. Ducuing, and P. S. Pershan, "Interactions between light waves in a nonlinear dielectric," Phys. Rev. **127**, 1918 (1962).

[41] D. A. Kleinman, A. Ashkin, and G. D. Boyd, Phys. Rev. **145**, 338 (1966)

[42] W. T. Silfvast, *Laser Fundamentals* (Cambridge U. Press, 1996), 340

[43] B. Dahmani, L. Hollberg and R. Drullinger, "Frequency stabilization of semiconductor lasers by resonant optical feedback," Opt. Lett., **12**, 876-878 (1987)

[44] Peter Buch and Peter Kohns, " Optically self-locked semiconductor laser with servo control for feedback phase and laser current," IEEE J. Quantum Elect. **Vol. 27** 1863-1868 (1989)

[45] Sin-ichi Ohshima and Harald Schnatz, " Optimization of injection current and feedback phase of an optically self-locked laser diode," J. Appl. Phys. **71**, 3114-3117 (1992)

[46] Dixon-GJ; Tanner-CE; Wieman-CE, "432-nm source based on efficient second-harmonic generation of GaAlAs diode-laser radiation in a self-locking external resonant cavity", Opt. Lett. **14**, 731-733 (1989)

[47] B. Dahmani, L. Hollberg and R. Drullinger, "Frequency stabilization of semiconductor lasers by resonant optical feedback", Opt. Lett., **12**, 876-878 (1987)

[48] This equation is obtained by carrying out the integration

$$\sqrt{m} = \left(\frac{2}{\sqrt{2\pi}}\right)^2 \frac{1}{\sqrt{\omega_x \omega_y \omega_{cx} \omega_{cy}}} \int_{-\infty}^{\infty}\int dxdy \cdot e^{-\frac{x^2}{\omega_x^2}} e^{-\frac{y^2}{\omega_y^2}} e^{-\frac{x^2}{\omega_{cx}^2}} e^{-\frac{y^2}{\omega_{cy}^2}}$$

[49] A. Hemmerich, D. H. McIntyre, C. Zimmerman and T. W. Hansch, "Second-harmonic generation and optical stabilization of a diode laser in an external ring resonator", Opt. Lett.**15**, 372-374 (1990)

[50] Y. Hadjar, F. Ducos, and O. Acef, "Stable 120-mW green output tunable over 2 THz by a second-harmonic generation process in a KTP crystal at room temperature," JOSB **25**, 1367-1369 (2000)

[51] Pascal Besnard, B. Meziane and Guy Michel Stephan, "Feedback phenomena in a semicon-ductor laser induced by distant reflectors", IEEE J. Quantum Electron., Vol. **QE-29**, 1271-1284 (1993)

[52] E. S. Polzik and H. J. Kimble, "Frequency doubling with $KNbO_3$ in an external cavity", Opt. Lett.**16**, 1400-1402 (1991)

[53] Motoichi Ohtsu, *Highly Coherent Semiconductor Lasers* (Artech House, Inc., 1992)

APPENDICES

APPENDIX A

EFFECTIVE CAVITY DISTANCE WITH A TILTED CRYSTAL

In this Appendix we will calculate the effective distance as paraxial rays propagates through the crystal. This will be needed to calculate how a Gaussian beam will propagate through the crystal. First we will review the calculation through a non-rotated crystal, which is a standard calculation given in many textbooks. Then we will calculate the case for a rotated crystal.

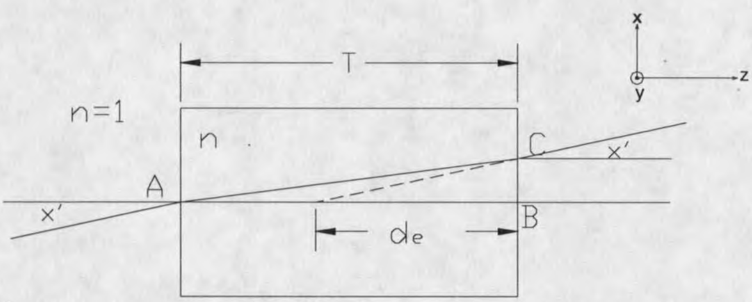

Figure-A. 1 The length of the crystal is T , and the refractive index is n . The transfer matrix is given by Equation A.2.

As illustrated in Figure-A.1, the central ray of the beam is normally incident at point A on the crystal of length T and refractive index n, and exits at point B. The paraxial beam with an angle x' enters the crystal at point A and exits the crystal at point C. Thus the paraxial ray appears to be propagating from a distance d_e. From Figure-A.1, it is easy to show that using Snell's law for small angle x':

$$d_e = \frac{BC}{x'} = \frac{T(x'/n)}{x'} = \frac{T}{n} \quad \text{A.1}$$

thus the transfer matrix for the crystal without rotation is given by[1,2]:

$$\begin{pmatrix} 1 & T/n \\ 0 & 1 \end{pmatrix} \quad \text{A.2}$$

If a Gaussian beam propagates through the crystal, the diameter and radius change of the beam will be the same as those when the beam propagates an effective distance $d_e = T/n$ in free space. This is the standard result that can be found in textbook[1,3].

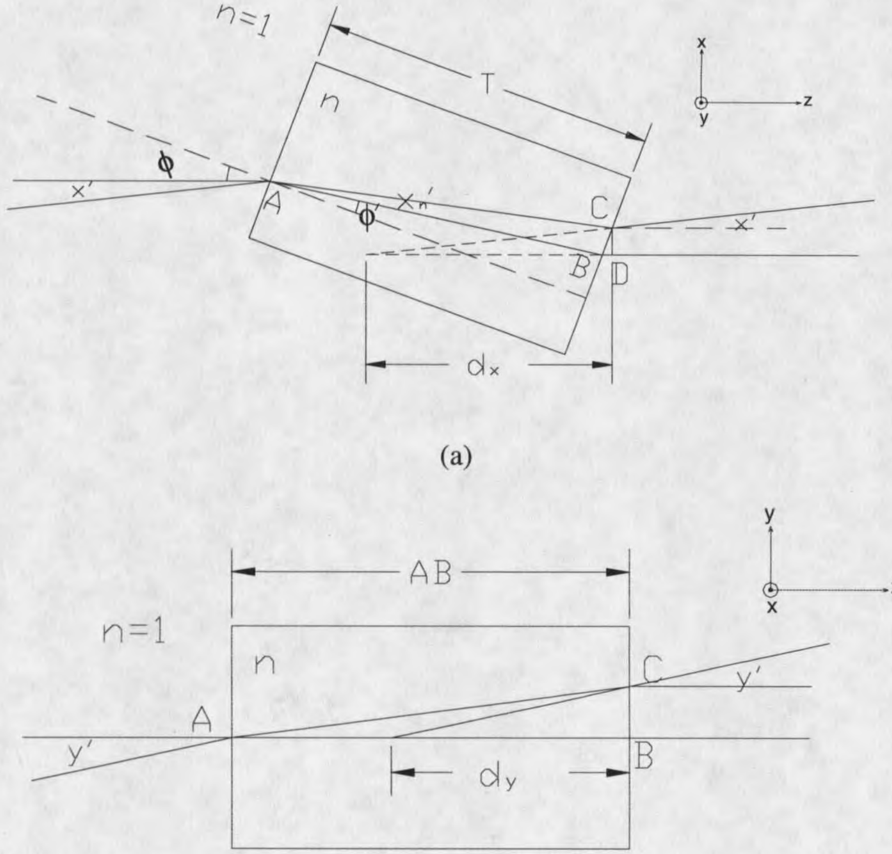

(a)

(b)

Figure-A. 2 The beam is propagating in the z − direction, and incident on the crystal with angle ϕ. (a) is the top view for horizontal plane. The paraxial ray has angle x' at point A in free space, x_n' in the crystal, and x' at point C in free space. d_x is the effective distance for the horizontal plane. (b) is the side view for the vertical plane. d_y is the effective distance for the vertical plane.

Now we consider the case of a rotated crystal. As illustrated in Figure-A.2, a beam is now incident on the crystal with an angle ϕ in the horizontal (xz) plane; (a) is the top view of the horizontal plane and (b) is the side view of the vertical plane. d_x and d_y are the effective distances in the vertical and the horizontal plane. From Figure-A.2 (a), the distance the central ray of the beam propagates is AB. For the paraxial beam in the vertical plane (Figure-A.2 (b)), the effective distance can be calculated using Equation A.1. However the distance that the central ray propagates through the crystal is AB which is given by:

$$AB = \frac{T}{\cos\phi'} = \frac{Tn}{\sqrt{n^2 - \sin^2\phi}} \qquad \text{A.3}$$

Thus using Equation A.1, the effective distance in the vertical plane is:

$$d_y = \frac{AB}{n} = \frac{T}{\sqrt{n^2 - \sin^2\phi}} \qquad \text{A.4}$$

In the horizontal plane (Figure-A.2 (a)) the effective distance is given by:

$$d_x = \frac{DC}{x'} = \frac{BC\cos\phi}{x'} \qquad \text{A.5}$$

From Figure-A.2 (a), we also find that for small angle x':

$$BC = T[\tan(\phi' + x_n') - \tan\phi'] = \frac{T}{\cos^2\phi'} x_n' = \frac{Tn^2}{n^2 - \sin^2\phi} x_n' \qquad \text{A.6}$$

and thus

$$x_n' = \frac{\cos\phi}{\sqrt{n^2 - \sin^2\phi}} x' \qquad \text{A.7}$$

Therefore the effective distance in the horizontal plane is

$$d_x = \frac{Tn^2(1-\sin^2\phi)}{(n^2-\sin^2\phi)^{3/2}} \qquad \text{A.8}$$

Thus we get the effective distance d_x and d_y in Equation 2.11.This result is the same as that given by REF[4] derived by Gaussian beam propagation, but the details of their derivation are not given.

Finally, the effective distance between the two curved mirrors, as illustrated in Figure-A.3, can be calculated using:

$$L_e = CA + d_e + BD = L - T' + d_e \qquad \text{A.9}$$

where d_e represent either d_x or d_y. It is easy to show that

$$T' = AB\cos(\phi-\phi') = T\sqrt{1-\sin^2\phi} + \frac{T\sin^2\phi}{\sqrt{n^2-\sin^2\phi}} \qquad \text{A.10}$$

Thus we obtain Equation 2.12. We also can see that the effective distance between the two curved mirrors is independent of the position of the crystal.

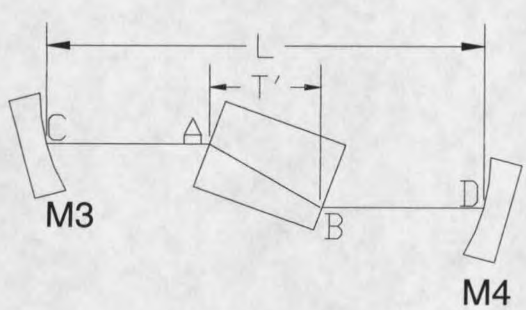

Figure-A. 3 The effective distance between the two curved mirrors.

APPENDIX B

PLANE WAVE IN ANISTROPIC MEDIA

In a linear anisotropic dielectric medium, the linear polarization is:

$$\vec{D} = \varepsilon \vec{E} \tag{B.1}$$

ε is the electric permittivity tensor. In the principle dielectric coordinate system ε can be written as:

$$\varepsilon = \begin{pmatrix} n_x^2 & 0 & 0 \\ 0 & n_y^2 & 0 \\ 0 & 0 & n_z^2 \end{pmatrix} \tag{B.2}$$

For a monochromatic plane wave traveling in an arbitrary direction $\hat{k}$ in an anisotropic crystal, with $\hat{k} = \sin\theta\cos\phi\hat{X} + \sin\theta\sin\phi\hat{Y} + \cos\theta\hat{Z}$, the Maxwell's equations are:

$$\begin{aligned} \vec{k}\times\vec{H} &= -\omega\vec{D} \qquad & \vec{k}\cdot\vec{D} &= 0 \\ \vec{k}\times\vec{E} &= \omega\mu_0\vec{H} \qquad & \vec{k}\cdot\vec{H} &= 0 \end{aligned} \tag{B.3}$$

Thus $\vec{k}$ is perpendicular to both $\vec{D}$ and $\vec{H}$. $\vec{H}$ is perpendicular to $\vec{k}$, $\vec{D}$ and $\vec{E}$. $\vec{k}$, $\vec{D}$ and $\vec{E}$ are in the same plane. We could write $\vec{E} = \vec{E}_T + \vec{E}_L$, where $\vec{E}_T$ is the transverse component perpendicular to $\vec{k}$, and $\vec{E}_L$ is the longitudinal component parallel to $\vec{k}$. Thus $\vec{D}$ is parallel to $\vec{E}_T$, with

$$D = n^2(\vec{k})E_T \tag{B.4}$$

where the refractive index $n(k)$ satisfies the equation[1,5]:

$$\frac{\sin^2\theta\cos^2\phi\cdot n^2(\vec{k})}{n^2(\vec{k})-n_x^2} + \frac{\sin^2\theta\sin^2\phi\cdot n^2(\vec{k})}{n^2(\vec{k})-n_y^2} + \frac{\cos^2\theta\cdot n^2(\vec{k})}{n^2(\vec{k})-n_z^2} = 1 \tag{B.5}$$

This equation has two solutions, $n(k) = n_a$ and n_b, corresponding to two eigenmodes with electric fileds $\vec{E}_a$ and $\vec{E}_b$ which have orthogonal displacement direction $\hat{D}_a$ and $\hat{D}_b$.

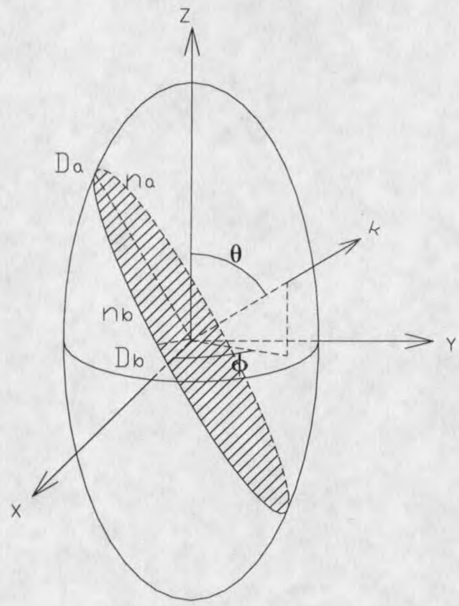

Figure-B.1 For a plane wave traveling in direction $\hat{k}$, the two eigenmodes displacement direction $\hat{D}_a$ and $\hat{D}_b$ are orthogonal, and the refractive index are n_a and n_b. XYZ are the principal axes.

For each of the eigenmode electric field $\vec{E}$, the wave equation can be written:

$$\nabla^2 E_T - \omega^2 \mu_0 \varepsilon_0 n^2(k) E_T = 0 \qquad \text{B.6}$$

thus the longitudinal component $\vec{E}_L$ is dropped from the wave equation, and the vector wave equation becomes a scalar wave equation.

The walk-off angle ρ is the angle between the wave vector $\vec{k}$ and the Poynting vector $\vec{S}=\frac{1}{2}\vec{E}\times\vec{H}*$. From the fact that $(\vec{D}\times\vec{H})//(\vec{E}_T\times\vec{H})//\vec{k}$, we have:

$$\tan\rho=\frac{E_L}{E_T} \qquad \text{B.7}$$

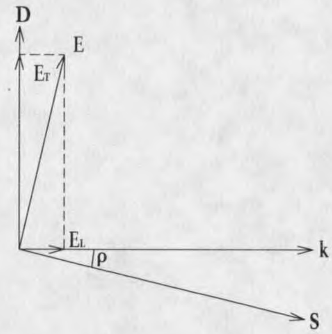

Figure-B.2 Relations of $\vec{S}$, $\vec{k}$, $\vec{D}$, $\vec{E}$ and $\vec{H}$. $\vec{H}$ is perpendicular to $\vec{S}$, $\vec{k}$, $\vec{D}$ and $\vec{E}$, the angle between $\vec{S}$ and $\vec{k}$ is the walk-off angle ρ.

For most of the anisotropic crystals, the difference between the principal index n_x, n_y and n_z are small, and it is easy to show that the walk-off angle is small. Thus the longitudinal component $\vec{E}_L$ is much smaller than the transverse component $\vec{E}_T$, and we can use E to replace E_T in Equation B.6.

In uniaxial crystals, $n_x=n_y=n_o$ and $n_z=n_e$. It is easy to show that the two eigenmodes displacement directions are:

$$\hat{D}_a=-\cos\theta\cos\phi\hat{X}-\cos\theta\sin\phi\hat{Y}+\sin\theta\hat{Z} \qquad \text{B.8}$$

with the refractive index $n_a=n_\theta$ that can be calculated using:

$$\frac{\sin^2\theta}{n_e^2}+\frac{\cos^2\theta}{n_o^2}=\frac{1}{n_\theta^2} \qquad \text{B.9}$$

Thus the refractive index varies with the propagating angle θ, the beam with polarization direction of $\hat{D}_a$ is known as extraordinary wave (e-wave).

The second displacement direction is

$$\hat{D}_b=\sin\phi\hat{X}-\cos\phi\hat{Y} \qquad \text{B.10}$$

with the refractive index $n_b=n_o$. Thus the refractive index is constant regardless of the propagating direction., this wave is known as ordinary wave (o-wave).

For the e-wave, the electromagnetic field E will has both a transverse component E_T and a longitudinal component E_L. The walk-off angle is:

$$\rho\approx\tan\rho=\frac{E_L}{E_T}=\frac{(n_e^2-n_o^2)\tan\theta}{n_o^2\tan^2\theta+n_e^2}=\frac{(\gamma^2-1)\tan\theta}{\tan^2\theta+\gamma^2} \qquad \text{B.11}$$

with $\gamma=\dfrac{n_e}{n_o}$.

Only the magnitude of ρ is considered in B.11. The direction of the walk-off is always toward the axis that has a bigger principle refractive index.

For the o-wave, the electromagnetic field E will only have transverse component E_T, and will behave as propagating in an isotropic media with a refractive index n_o.

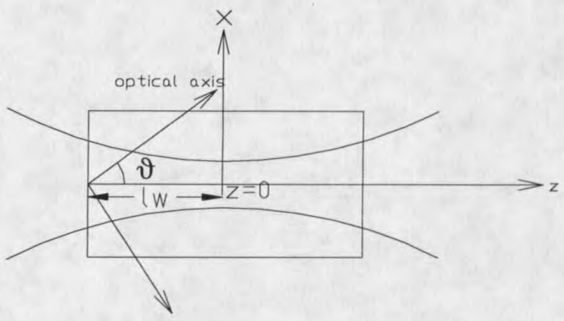

Figure-B.3 Gaussian beam propagation in a uniaxial crystal.

As illustrated in Figure-B.3, if a one-dimension Gaussian beam is incident on a uniaxial crystal with angle ϑ between the propagation direction and the optical axis Z, the direction of E is such that only the e-wave is produced in the crystal, the electromagnetic field at the front surface is:

$$E(x, z=-l_w^-) = \frac{E_0}{\sqrt{1+i\zeta_x}} \exp\left[-\frac{x^2}{\omega_{0,x}{}^2(1+i\zeta_x)}\right] \qquad \text{B.12}$$

with $\zeta_x = 2l_w / b_x$. The confocal parameter $b_i = k_0 \omega_{0,x}{}^2$, and the Fourier transformation is

$$\tilde{e}(k_x, z=-l_w^-) = E_0 \sqrt{\pi}\omega_0 \exp\left[-\frac{k_x^2}{(2/\omega_0)^2}\right] \exp\left(-i\sqrt{k_0{}^2 - k_x^2}\, l_w\right) \qquad \text{B.13}$$

Thus inside the crystal the electromagnetic filed is:

$$E(x,z) = \frac{1}{2\pi}\int_{-\infty}^{\infty} dk_x e^{ik_x x} \frac{1}{n}\tilde{e}(k_x, z=-l_w^-) \exp\left(i\cdot(z+l_w)\sqrt{k_0{}^2 n^2(k_x) - k_x^2}\right) \qquad \text{B.14}$$

with $n = \dfrac{n_e}{\sqrt{\sin^2\vartheta + \gamma^2\cos^2\vartheta}}$ from Equation B.9.

and $n(k_x) = n(\vartheta - \frac{k_x}{k_0 n}) = n(\vartheta) - \frac{dn}{d\theta}\bigg|_{\theta=\vartheta} \cdot \frac{k_x}{k_0 n} = n(1 - \rho\frac{k_x}{k_0 n})$.

$$\sqrt{k_0{}^2 n^2(k_x) - k_x^2} \approx \sqrt{k_0{}^2 n^2 (1 - 2\rho\frac{k_x}{k_0 n}) - k_x^2} \approx k_0 n - \frac{2\rho k_0 n k_x + k_x^2}{2k_0 n}$$

We have:

$$E(x,z) = \frac{E_0}{n}\frac{e^{i[k_0 nz + k_0(n-1)l_w]}}{\sqrt{1+i\zeta}}\exp\left[-\frac{[x-\rho(z+l_w)]^2}{\omega_{0,x}{}^2(1+i\zeta)}\right] \qquad \text{B.15}$$

with $\zeta = \frac{2[z-(n-1)l_w]}{b}$, and $b = k_0 n \omega_{0,x}{}^2$. Thus the beam waist will located at $z = (n-1)l_w$ instead of $z = 0$. The peak of the Gaussian beam moves along $x = \rho(z + l_w)$ instead of $x = 0$. These facts can also be used to check the numerical simulation.

APPENDIX C

POTASSIUM NIOBATE ($KNBO_3$) CRYSTAL

The properties of the Potassium Niobate ($KNbO_3$) crystal has been discussed in REF[6] and [7].We follow their notations.

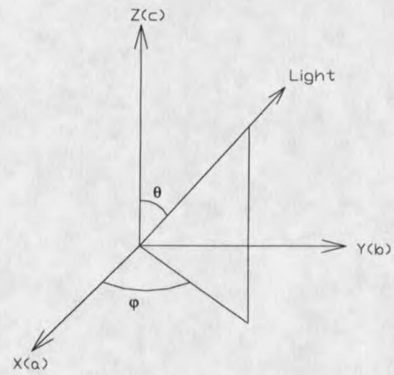

Figure-C.1 The crystal coordinate system of the $KNbO_3$ crystal. The principle $X(a)$, $Y(b)$ and $Z(c)$ axes are labeled according to $n_b > n_a > n_c$.

The dispersion relations of the principle refractive index are:

$$n_a = \sqrt{4.8355 + \frac{0.12839}{\lambda^2 - 0.056342} - 0.025379 \cdot \lambda^2}$$

$$n_b = \sqrt{4.9873 + \frac{0.15149}{\lambda^2 - 0.064143} - 0.028775 \cdot \lambda^2} \qquad \text{C.1}$$

$$n_c = \sqrt{4.4208 + \frac{0.10044}{\lambda^2 - 0.054084} - 0.019592 \cdot \lambda^2}$$

The temperature dependent dispersion relations can be found in REF[6]

The nonlinear susceptibility tensor is:

$$d = \begin{pmatrix} 0 & 0 & 0 & 0 & d_{31} & 0 \\ 0 & 0 & 0 & d_{32} & 0 & 0 \\ d_{31} & d_{32} & d_{33} & 0 & 0 & 0 \end{pmatrix} \qquad \text{C.2}$$

The nonlinear coefficients at λ=1064nm are:

$$\begin{aligned} d_{31} &= \text{-11.9pm/V} \\ d_{32} &= \text{-13.7pm/V} \\ d_{33} &= \text{-20.6pm/V} \end{aligned} \qquad \text{C.3}$$

For the SHG near 970nm, the fundamental light will propagate in X-Y plane and the polarization will also be in the X-Y plane. The wave vector is $\hat{k} = \hat{X}\cos\varphi + \hat{Y}\sin\varphi)$, and the fundamental electromagnetic field is $\vec{E}^{(\omega)} = E^{(\omega)}(\hat{X}\sin\varphi - \hat{Y}\cos\varphi)$. The nonlinear polarizations are defined as:

$$\vec{P}^{(2\omega)} = E^{(\omega)^2}\begin{pmatrix} 0 \\ 0 \\ d_{31}\sin^2\varphi + d_{32}\cos^2\varphi \end{pmatrix} \qquad \text{C.4}$$

$$\vec{P}^{(\omega)} = \begin{pmatrix} 2d_{31}\sin\varphi E^{(\omega)^*}E^{(2\omega)} \\ 2d_{32}\cos\varphi E^{(\omega)^*}E^{(2\omega)} \\ (d_{31}\cos^2\varphi + d_{32}\sin^2\varphi)E^{(\omega)^2} + d_{33}E^{(2\omega)^2} \end{pmatrix} \qquad \text{C.5}$$

The effective nonlinear coefficient is defined by:

$$\vec{P}^{(2\omega)} \cdot \hat{e}_2 = d_{eff}E^{(\omega)^2} \qquad \text{C.6}$$

The effective nonlinear coefficient d_{eff} for SHG near 970nm is

$$d_{eff} = d_{31}\sin^2\varphi + d_{32}\cos^2\varphi \qquad \text{C.7}$$

The phase matching conditions had been discussed in REF[6], for convenience, the phase matching condition at 968nm-976nm is plotted in Figure-C.2. (a) is the temperature dependence of the wavelength at $\varphi = 72°$. (b) is φ dependence of the wavelength at 22°C.

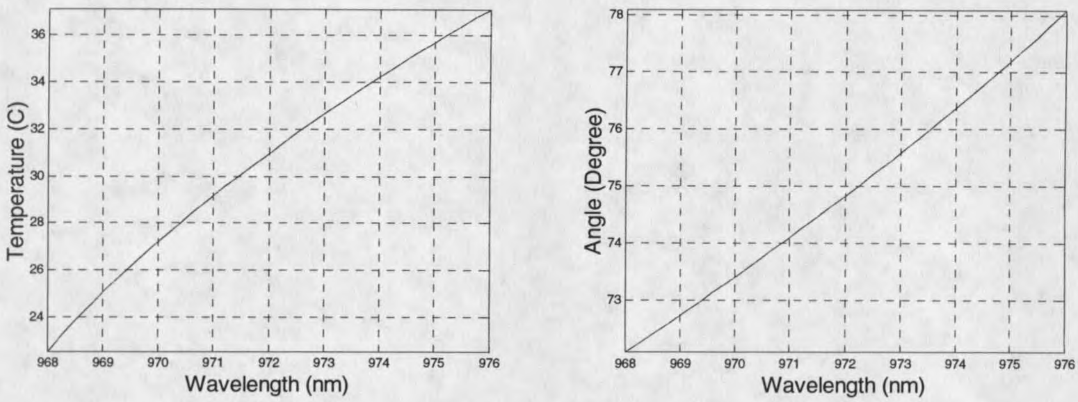

Figure-C.2 The phase matching condition at 968nm-976nm. (a)Temperature with wavelength at $\varphi = 72°$. (b) φ with wavelength at 22°C.

Thus to achieve phase matching condition at 968nm-976nm, we can use a b-cut[8] crystal with the angle of incidence of the beam about 40°.

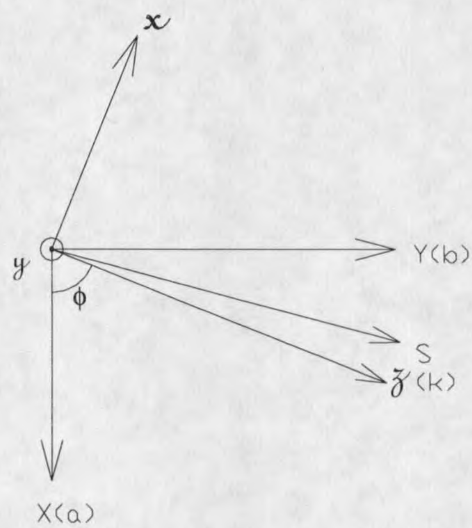

Figure-C.3 Coordinate system of the simulation and the crystal principle axes.

The xyz coordinate system of the SHG simulation is defined so that the z -axis is along the direction of the beam propagation k , the x -axis is in the X-Y plane, and the y -axis is along Z, as illustrated in Figure-C.2. The walk-off direction is toward Y(b)-axis, e.g. $+x$ direction.

APPENDIX D

SIMULATION PROGRAMS

The following are the MATLAB programs we used in the simulation, and can be down loaded from: http://www.physics.montana.edu/students/xsun/program/

Phase matching of $KNbO_3$:

```
angles.m
n.m
newave.m
transcon.m

criticalT.m
nKNbO3.m
nwn2w.m

deffq.m
```

Curve fitting:

```
fitgauss.m
fitgauss_01.m
fitgauss_02.m
fgauss.m

fitgaussian.m
fitgaussian_01.m
fitgaussian_02.m
fgaussian.m

waist2.m
waist3.m
maxpostion.m
```

SHG Calculation:

```
Gaussian.m
Dangle.m
SHGcal.m
SHGincrease.m
dEdz.m

Efphase.m
E2fphase.m

dP2w.m
M2_w0.m
mDdk.m
MDdk_fit.m
```

```
MDdk_w0.m
P2w_Dk.m
P2w_lw.m
P2w_w0.m
Ptop2w.m
```

Cavity mode calculation:

```
ringw.m
ringwd.m
ringsil.m
findrat.m
```

References of appendices

[1] Amnon Yariv, "Quantum Electronics", 3rd edition, (John Wiley and Sons, New York, 1989)

[2] H. Hogelink and T. Li, "Laser beams and resonators", Proc. IEEE, Vol. 54, No. 10, 1312-1329 (1966)

[3] A. E. Siegman, "Lasers", (University Science Books, 1986)

[4] D. C. Hanna, "Astigmatic Gaussian beams produced by axially asymmetric laser cavities," IEEE J. Quantum Electron., Vol. QE-5, 483-488 (1969)

[5] Bahaa E.A. Saleh, M. C. Teich, "Fundamentals of Photonics", 1st edition, (John Wiley and Sons, New York, 1991)

[6] B. Zysset, I. Biaggio, and P. Gunter, "Refractive indices of orthorhombic $KNbO_3$. I. Dispersion and temperature dependence," JOSB **Vol. 9** 380-386 (1992)

[7] I. Biaggio, P. Kerkoc, L. S. Wu, P. Gunter, and B. Zysset, "Refractive indices of orthorhombic $KNbO_3$. II. Phase-matching configurations for nonlinear-optical interactions," JOSB **Vol. 9** 507-517 (1992)

[8] The cleaved surfaces are perpendicular to b-axis, and the beam is incident on these surfaces. This usage can be found in the catalogs of VLOC Inc. and Sepctragen, etc.